Coupled field modeling of thermoresponsive hydrogels with upper/lower critical solution temperature

A. Valverde-González[a,b,c], J. Reinoso[b,d,e], M. Paggi[a], B. Dortdivanlioglu[c,f,*]

[a] *IMT School for Advanced Studies Lucca, Piazza San Francesco 19, Lucca 55100, Italy*
[b] *Grupo de Ingeniería de Estructuras y Materiales. Departamento de Mecánica de Medios Continuos y Teoría de Estructuras, ETS Ingeniería, Universidad de Sevilla, Camino de los Descubrimientos S/N, 41092 Seville, Spain*
[c] *Civil, Architectural and Environmental Engineering, The University of Texas at Austin, Austin, 78712, TX, USA*
[d] *Escuela Politécnica Superior, Universidad de Sevilla, C/ Virgen de África, 7, Sevilla, 41011, Spain*
[e] *ENGREEN - Laboratory of Engineering for Energy and Environmental Sustainability, Universidad de Sevilla, Seville, Spain*
[f] *Oden Institute for Computational Engineering and Sciences, The University of Texas at Austin, Austin, 78712, TX, USA*

Abstract

An inf-sup stable FE formulation for the thermo-chemo-mechanical simulation of thermoresponsive hydrogels is herein proposed by approximating the displacement field via quadratic shape functions and both the chemical potential (fluid pressure) and the temperature fields by linear functions. The formulation is implemented into a stable thermo-chemo-mechanical user-element subroutine (`UEL`) in Abaqus, denoted as `Q2Q1Q1`. The proposed formulation has been validated in relation to thermoresponsive hydrogels to interpret several examples of transient diffusion-driven swelling deformations. First, the upper/lower critical solution temperature behaviors of thermoresponsive hydrogels has been captured, studying several peculiarities comprising the diffusion length influence at the instantaneous loading state and the overlooked influence of the mass flux and the hyperelastic stretching on the temperature field. Subsequently, the analysis has been conducted to investigate the impact of temperature-dependent swelling ratio on the mechanical behavior of spheres undergoing compression. Moreover, the accuracy has been assessed by numerically replicating the seminal experiments that explore the influence of cross-linking density on the thermally driven swelling of *PNIPAAm* hydrogels.

Keywords: Thermoresponsive hydrogels; Inf-sup stability; Mixed Finite Element formulation; Critical solution temperature; Hydrogel swelling

1. Introduction

Hydrogels are elastic polymeric networks that can absorb large quantities of water and consequently show reversible large swellings. Their applications are widespread ranging from smart valves [1–3], sensors [4–7], tissue engineering [8–11], to drug delivery systems [12–16]. The reason behind this displayed versatility is related to their ability to withstand large deformations combined with the dependence of their mechanical response on environmental changes such as chemical fields and pH [17, 18], electric fields [19, 20], light [21, 22], humidity [23, 24] and temperature [25–27], among others. Focusing on the latter property, there exists a subclass of hydrogels called *thermoresponsive hydrogels*, which exhibit large swelling when being heated above or cooled down a critical temperature. The former ones exhibit an upper critical solution temperature (UCST) point, belonging to this behavior natural hydrogels such as like agarose, agar, collagen and gelatin [28–30]. On the other side, hydrogels exhibiting a lower critical solution temperature (LCST)

*Corresponding author.
Email address: `berkin@utexas.edu` (B. Dortdivanlioglu)

swells when they are cooled below the typical temperature, being framed within this pattern considerably employed hydrogels like poly(N-isopropylacrylamide) (*PNIPAAm*) [31–34] and polyethylene glicol (PEG) [35–37], among others. The proposed framework is able to analyze the complex LCST and UCST behaviors.

Within the field of Computational Mechanics, a comprehensive examination is conducted on the proposed Finite Element/eXtended-Finite Element methods (FEM/XFEM) simulations of the equilibrium swelling of gels. In the first place, the seminal works by Dolbow et al. [38] and Ji et al. [39] set the stage for continuum models modelling chemically and thermally induced volume transitions in hydrogels, respectively, by employing the XFEM combined with the Element-Set technique. This approach establishes the coupling between the deformation and solute concentration solely through the interfacial normal configurational force balance. Subsequently, Hong et al. [40, 41] takes a step forward by formulating the thermodynamics problem considering the coupling between the large deformation and the diffusion problems. Based on this approach, the variational formulation derived by Kang and Huang [42] and the pivotal works by Chester and Anand, first for isothermal problems [43], and, then for, thermoresponsive hydrogels [44] establish the landmark in considering the problem of hydrogel swelling as a coupled deformation-diffusion problem by developing a constitutive theory consistent with the basic mechanical balance laws and the balance law for the fluid content and implementing it into a commercial Finite Element (FE) package. This means that, for the numerical modeling of a thermoresponsive behavior of gels, the displacement, the chemical field and the temperature require separate approximation as the primary field driving forces of the chemo-thermomechanical problem [45–47].

The short time behavior of hydrogels make them resemble a fully incompressible or quasi-incompressible hyperelastic materials, as the diffusion of water occurs on a longer timescale. To tackle this, mixed methods are adopted to solve volumetric locking issues related to the incompressible limit, such as the F-bar method developed by de Souza Neto et al. [48] that is implemented in the referential work from Chester and Anand [44]. However, these papers do not address that the independent discretization of primary fields carries the risk of the appearance on severe oscillations in the solution of the chemical potential field, thus resulting in a violation of the Ladyzshenskaya-Babuška-Brezzi (LBB) condition, also called the *inf-sup* condition [49–52]. When this condition is not met, spurious oscillations in the chemical potential field start to arise which can serve as perturbations to trigger mechanical instabilities for the response of a nearly incompressible poroelastic medium. In addition to these instability effects, Murad and Loula [53] and Wan [54] state that there are also numerical oscillations dominant in the early stage of transient responses due to sharp boundary conditions, which would decay in time and eventually converge towards the equilibrium of the problem. Therefore, for hydrogel formulations with a fully coupled chemo-mechanical nature, modeling the continuous mass flow is required the usage of special order interpolations to satisfy the balance of mass and, at the same time, fulfill the LBB conditions. Some examples of stable mixed FE applied for hydrogels can be observed in the mixed element formulation based on the Enhanced Assumed Strain technique developed by Krischok and Linder [55] or in the multiple works carried out by Bouklas et al. [56, 57] where it is employed a standard Taylor-Hood element [58] with quadratic displacement and a linear chemical potential field. Efficient subdivision-stabilized mixed isogeometric models of hydrogels also exist [52, 59]. Notably, in these formulations, Chester and Anand [44] disregard the dependence of the temperature variation due to fluid flow and elastic stretching in the hydrogel mechanical behavior, which we demonstrate as a prevailing effect is the coupling is present. Several experiments elucidating the swelling behavior have underscored this intricate interplay between the mechanical and thermal fields [60–62].

In this work, we are modelling a fully-coupled numerically stable thermo-chemo-mechanical FE in order to study the complex material behavior of thermoresponsive hydrogels along several examples of transient diffusion-driven swelling deformations. For this pursuit, we present a three-field mixed FE element that approximates the displacement via quadratic shape functions and both the chemical potential and the temperature by linear shape functions, denoted as `Q2Q1Q1`. Throughout this paper, the proposed formulation will be validated through its capacity to accurately depict the LCST and UCST behaviors exhibited by the thermoresponsive hydrogels. Subsequently, it will be used from a quantitative standpoint to address, initially, its robustness with the study of spheres subject to compressive load under different temperatures; and then, its accuracy in capturing the free swelling experimental tests carried out by Oh et al. [63] with various crosslinking concentrations. This paper aims to contribute to the field of Computational Mechanics by

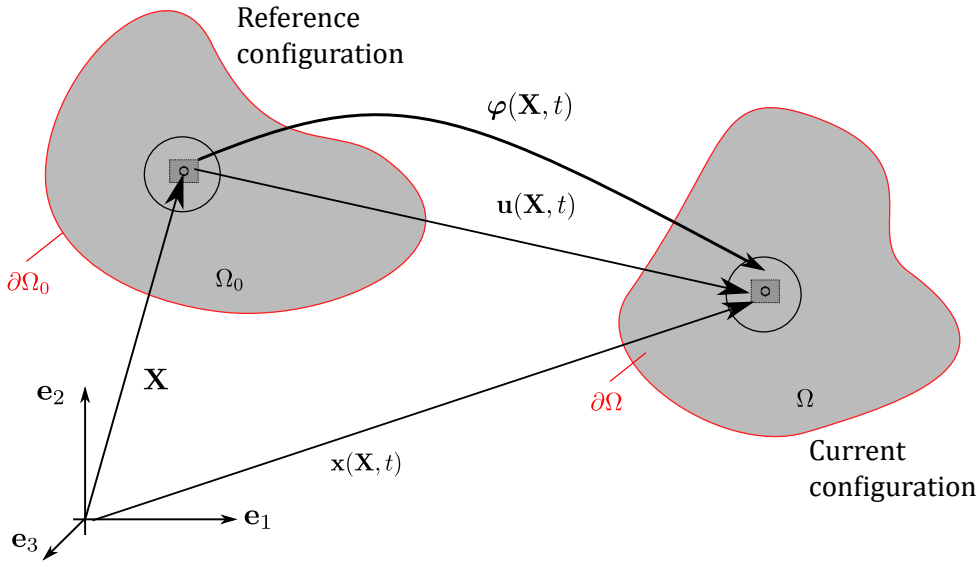

Figure 1: Deformation process from the reference configuration to the current one.

including an inf-sup stable formulation for the modeling of thermoresponsive hydrogels. It also demonstrates the accuracy of this approach by resolving and capturing representative experimental problems.

The paper is structured as follows. The basic concepts where the three-field problem and the local equations are introduced is included in Section 2. Section 3 displays the development of the balance of energy to shape the constitutive behavior and the material model and the derivation of the formulation to introduce the weak form of the problem. Further insight on the implementation is provided in Section 4, where the `Q2Q1Q1` element is presented to model the problem of thermoresponsive hydrogels. Efforts delineated in Section 5 are directed to simulate numerical examples, first to verify the proposed numerical formulation and then, into more intricate problems, to test its functionality in checking the temperature dependence on compressive tests and reproducing numerical experiments concerning the influence of cross-linking in thermal-dependent swelling. Some final remarks and conclusions are provided in Section 6.

2. Theoretical formulation

This section outlines the fundamental concepts and definitions of the current numerical framework addressing the use of a mixed displacement-mass diffusion-temperature formulation for the large deformation analysis of diffusion in solids. The ultimate goal is to specialize this formulation for the analysis of thermoresponsive hydrogels.

2.1. Basic definitions

Complying with standard non-linear Continuum Mechanics, let an arbitrary spatial point defined in the current configuration be defined as $\mathbf{x} := \boldsymbol{\varphi}(\mathbf{X},t)$, being $\boldsymbol{\varphi}(\mathbf{X},t)$ the non-linear deformation map which projects the material points $\mathbf{X}$ from the initial configuration $\Omega_0 \subset \mathbb{R}^n$ to the current one $\Omega \subset \mathbb{R}^n$ (where n is the dimension of analysis). This transformation is plotted in Fig. 1. The transformation of the differential line elements throughout the deformation process is characterized by the deformation gradient $\mathbf{F}$ whose definition renders

$$\mathbf{F} := \nabla_{\mathbf{X}} \boldsymbol{\varphi}(\mathbf{X},t) = \frac{\partial \boldsymbol{\varphi}(\mathbf{X},t)}{\partial \mathbf{X}} = \frac{\partial \mathbf{x}}{\partial \mathbf{X}} \tag{1}$$

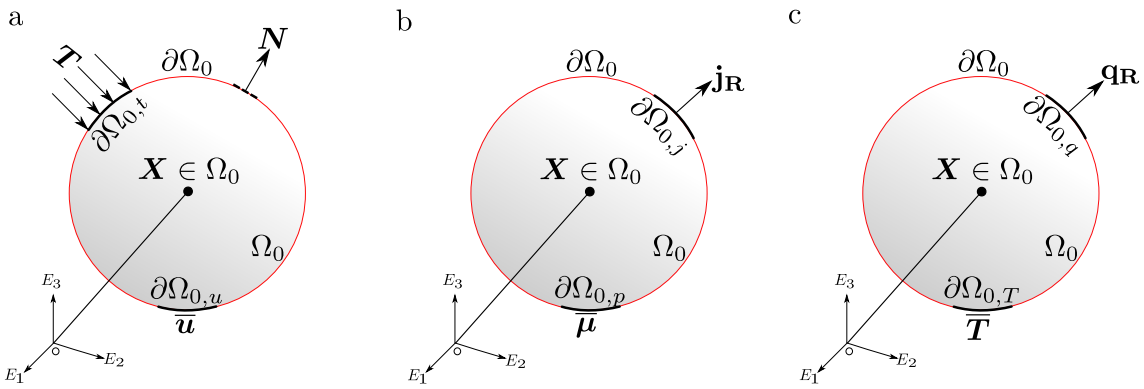

Figure 2: Schematic representation of the three-field boundary value problem: (a) displacement, (b) mass transport, and (c) temperature.

The Jacobian, i.e. the ratio of the deformed to the undeformed volume, being the determinant of $\mathbf{F}$ shall fulfill the condition of $J = \det[\mathbf{F}] > 0$.

The boundary-value problem for the modelling of this problem is treated as a coupled four-field problem, characterized by the displacement field $\mathbf{u}$, the concentration field C, the chemical potential μ and the temperature T. Variational approaches are proposed for thermomechanical and dissipative solids, e.g., in [64, 65] and deformation-diffusion problems, e.g., in [66]. Following the approach in [66], the transition from a Cahn-Hilliard-type model to a standard Fickian-type model is achieved through the degeneration of the definition of the chemical potential. As the chemical potential drives the flux $\dot{C}$ of the species, this transformation is made by optimizing the chemical potential with respect to the concentration, performing its local update at the integration points, defining a condensed incremental potential that only depends on the displacement field and the chemical potential. The reader is referred to [66] for further information regarding this operation.

Following the scheme plotted in Fig. 2, we make a brief description of the problem for both three fields. Starting from a mechanical perspective, in order to track the motion of the body from the material to the spatial configuration at time t, the displacement vector is defined as:

$$\mathbf{u}(\mathbf{X}, t) := \mathbf{x}(\mathbf{X}, t) - \mathbf{X} \tag{2}$$

Accordingly, the right and left Cauchy-Green tensors are obtained as, respectively:

$$\mathbf{C} := \mathbf{F}^{\mathrm{T}} \cdot \mathbf{F}; \quad \mathbf{b} := \mathbf{F} \cdot \mathbf{F}^{\mathrm{T}} \tag{3}$$

The delimiting surface of the body is decomposed into two regions: one where the displacements $\mathbf{u}$ are prescribed through Dirichlet-type boundary conditions (BCs), $\partial\Omega_{0,u}$ and one where the nominal tractions $\mathbf{T}$ are prescribed via a Neumann-type BC, $\partial\Omega_{0,t}$, such that $\partial\Omega = \partial\Omega_{0,u} \cup \partial\Omega_{0,t}$ and $\partial\Omega_{0,u} \cap \partial\Omega_{0,t} = \emptyset$. For the Neumann condition, we can establish a linear dependency between the nominal traction vector $\mathbf{T}$ and the reference normal outward $\mathbf{N}$ through the following theorem

$$\mathbf{T} = \mathbf{P} \cdot \mathbf{N} \tag{4}$$

where $\mathbf{P}$ is the first Piola-Kirchhoff stress tensor. Equivalently, the Cauchy stress tensor $\mathbf{P}$ can be defined via this theorem by performing a push-forward operation to refer to the current configuration Ω:

$$\mathbf{t} = \boldsymbol{\sigma} \cdot \mathbf{n} \quad \text{with} \quad \boldsymbol{\sigma} = J^{-1} \mathbf{P} \cdot \mathbf{F}^{\mathbf{T}} \tag{5}$$

The relation between Eqs. (4) and (5) is obtained by considering $\mathbf{T}\mathrm{d}A = \mathbf{t}\mathrm{d}a$. In order to compute a symmetric Langragian tensor, the second Piola-Kirchoff stress tensor $\mathbf{S}$ serves for this duty in the reference configuration and it reads as:

$$\mathbf{S} = \mathbf{F^{-1}} \cdot \mathbf{P} = J\, \mathbf{F^{-1}} \cdot \boldsymbol{\sigma} \cdot \mathbf{F^{-T}} \tag{6}$$

Moving to the diffusion problem, again, this can be divided into two sub-domains: one where the chemical potential μ is prescribed through a Dirichlet BC, $\partial\Omega_{0,p}$; and $\partial\Omega_{0,j}$, where we perform an analogous operation to the nominal tractions theorem (Eq. (4)) to obtain the referential species out-flux $\mathbf{j}_R$, that depends linearly on the outward normal $\mathbf{N}$

$$J_n = \mathbf{j}_R \cdot \mathbf{N} \tag{7}$$

where J_n denote the scalar mass flux. The spatial species flux $\mathbf{j}$ relies on a analogous relation to the Cauchy stress, therefore its definition yields as:

$$\mathbf{j} = J^{-1}\mathbf{F} \cdot \mathbf{j_R} \tag{8}$$

Assuming that the fluid transport follows a Fickian diffusion relation, we can establish a relation to obtain the nominal fluid flux $\mathbf{j_R}$ from the product of the mobility tensor $\mathbf{M}$ based on the gradient of the chemical potential:

$$\mathbf{j_R} = -\mathbf{M}\cdot\nabla_{\mathbf{X}}\mu \tag{9}$$

The remaining unknown in this three-field mixed-formulation problem is the thermal field and also can be traced into two sub-domains: the region $\partial\Omega_{0,T}$, where the temperature T is prescribed, and the region $\partial\Omega_{0,q}$, where the evolution of the heat flux $\mathbf{q_R}$ is applied considering the Stokes flux with the following definition

$$Q_n = \mathbf{q_R} \cdot \mathbf{N} \tag{10}$$

where Q_n denotes the scalar heat flux for the problem. Then, the spatial heat flux $\mathbf{q}$ can be obtained as

$$\mathbf{q} = J^{-1}\mathbf{F} \cdot \mathbf{q_R} \tag{11}$$

and then, by establishing a Fourier-type relation, we trace the value of $\mathbf{q_R}$ by the product of the thermal conductivity tensor $\mathbf{K}$ with the gradient of the temperature

$$\mathbf{q_R} = -\mathbf{K} \cdot \nabla_{\mathbf{X}} T \tag{12}$$

2.2. Local equations and balance of energy

The general equations that drive the coupled deformation-diffusion-temperature problem are presented in their local form for the reference configuration. Before the balance of total energy, we need to define some local balances for every field. The conservation of solid mass reads as:

$$\rho_0 = J\rho \tag{13}$$

where $\rho(\mathbf{x},t)$ and $\rho_0(\mathbf{X})$ are the density fields in the current and reference configuration, respectively. From here, we can obtain the material version of the balance of linear momentum, which adopts the form of:

$$\nabla_{\mathbf{X}} \cdot \mathbf{P} + \rho_0 \overline{\mathbf{F}}^V = \mathbf{0} \tag{14}$$

where the operator $\nabla_{\mathbf{X}} \cdot [\bullet]$ denotes the divergence with respect to the reference setting, and $\overline{\mathbf{F}}^V$ identifies the prescribed body forces per unit of reference volume.

For the mass transport, we consider C as the concentration of fluid content inside the hydrogel, i.e. the number of moles of fluid molecules absorbed by the polymer network, reckoned per unit volume of the dry reference configuration. For this field, the balance species content equation takes the local form of:

$$\dot{C} = -\nabla_{\mathbf{X}} \cdot \mathbf{j_R} \tag{15}$$

For the balance in the temperature, we refer to the entropy variable η_R by introducing the second law of thermodynamics as:

$$\dot{\eta_R} \geq -\nabla_{\mathbf{X}} \cdot \left[\frac{\mathbf{q_R}}{T}\right] + \frac{R}{T} \tag{16}$$

All this information that we collect for the three-field formulation global balance is plotted in the box below as a summary in the reference configuration for this quasi-static problem

1. Balance of solid mass:	$\rho_0 = J\rho$	(17a)
2. Balance of species content:	$\dot{C} = -\nabla_{\mathbf{X}} \cdot \mathbf{j_R}$	(17b)
3. Balance of entropy:	$\dot{\eta_R} \geq -\nabla_{\mathbf{X}} \cdot \left[\frac{\mathbf{q_R}}{T}\right] + \frac{R}{T}$	(17c)
4. Balance of linear momentum:	$\rho_0 \ddot{\boldsymbol{\varphi}} = \nabla_{\mathbf{X}} \cdot \mathbf{P} + \rho_0 \overline{\mathbf{F}}^V = \mathbf{0}$	(17d)
5. Constitutive stress:	$\mathbf{S} = 2\partial_{\mathbf{C}} \Psi(\mathbf{C}, C, T)$	(17e)
6. Chemical potential:	$\mu = \partial_C \Psi(\mathbf{C}, C, T)$	(17f)
7. Entropy:	$\eta_R = -\partial_T \Psi(\mathbf{C}, C, T)$	(17g)
8. Fourier's Law:	$\mathbf{q_R} = -\mathbf{K} \cdot \nabla_{\mathbf{X}} T$	(17h)
9. Fick's Law:	$\mathbf{j_R} = -\mathbf{M} \cdot \nabla_{\mathbf{X}} \mu$	(17i)

where $\bar{p}$ accounts as the fluid pressure and ν is the number of solvent molecules per volume reference unit. Our discussion of thermodynamics involves the following fields: the specific internal energy e, the second Piola-Kirchhoff stress $\mathbf{S}$, the heat flux per unit reference area $\mathbf{q_R}$, the external heat supply per unit reference volume R and the material flux of fluid molecules $\mathbf{j_R}$. With these magnitudes, the proposed DOFs and Eqs. (17a)-(17i) at hand, we can express the local form of the balance of the total energy like:

$$\rho_0 \dot{e} = \mathbf{S} : \dot{\mathbf{E}} - \nabla_{\mathbf{X}} \cdot \mathbf{q_R} + R + \mu \dot{C} - \mathbf{j_R} \cdot \nabla_{\mathbf{X}} \mu \tag{18}$$

where $\dot{\mathbf{E}}$ is the variation of the Green-Lagrange deformation tensor. The expression can be developed upon considering the second law of Thermodynamics, where the equation for the evolution of the entropy (Eq. (17c)) can be extended as:

$$\nabla_{\mathbf{X}} \cdot \left[\frac{\mathbf{q_R}}{T}\right] + \frac{R}{T} = \frac{1}{T}(R - \nabla_{\mathbf{X}} \cdot \mathbf{q_R}) + \frac{1}{T^2}\mathbf{q_R} \cdot \nabla_{\mathbf{X}} T \tag{19}$$

Then, by considering Legendre transformation: $\Psi = e - T\eta$, and Eq. (18), we reach the expression for the Clausius-Duhem inequality that guarantees the local consistency of the equation, where the local dissipated global potential $\mathcal{D}$ is expressed as:

$$\mathcal{D} = \mathbf{S} : \dot{\mathbf{E}} + \mu\dot{C} - \mathbf{j_R} \cdot \nabla_{\mathbf{X}}\mu - \frac{1}{T}\mathbf{q_R} \cdot \nabla_{\mathbf{X}} T - \rho_0(\dot{\Psi} + \dot{T}\eta) \geq 0 \tag{20}$$

Note that $\mathcal{D}$ can be split into three parts due to: (i) local actions $\mathcal{D}_{\text{loc}}$, (ii) heat conduction $\mathcal{D}_{\text{cond}}$ and (iii) mass diffusion $\mathcal{D}_{\text{dif}}$

$$\mathcal{D}_{loc} = \mathbf{S} : \dot{\mathbf{E}} + \mu\dot{C} - \rho_0(\dot{\Psi} + \dot{T}\eta) \geq 0 \tag{21a}$$

$$\mathcal{D}_{cond} = -\frac{1}{T}\mathbf{q_R} \cdot \nabla_{\mathbf{X}} T \geq 0 \tag{21b}$$

$$\mathcal{D}_{diff} = -\mathbf{j_R} \cdot \nabla_{\mathbf{X}}\mu \geq 0 \tag{21c}$$

where Eq. (21a) is known as the Clausius-Planck inequality, Eq. (21b) stands for the Fourier inequality and Eq. (21c) is an inequality to satisfy the chemical potential driving the fluid diffusion in hydrogels.

3. Constitutive formulation

3.1. Objective free energy function

The constitutive equations are constructed such that the dissipation condition plotted in Eq. (20) is a priori satisfied for all processes. The free energy is thought to depend on the primary variables and their gradients:

$$\Psi = \tilde{\Psi}(\mathbf{C}, \nabla_{\mathbf{X}}\mathbf{C}, C, \nabla_{\mathbf{X}} C, T, \nabla_{\mathbf{X}} T) \tag{22}$$

at $\mathbf{X} \in \Omega_0$. With a view towards determining the restrictions imposed by the local free energy imbalance (Eq. (20)), and by dismissing the minimal influence of primary gradients, the temporal rate of Eq. (22) can be expressed as:

$$\dot{\Psi} = \frac{\partial \Psi}{\partial \mathbf{C}}\dot{\mathbf{C}} + \frac{\partial \Psi}{\partial C}\dot{C} + \frac{\partial \Psi}{\partial T}\dot{T} \tag{23}$$

Substituting Eq. (23) into Eq. (20), we obtain:

$$\mathcal{D} = \left[\frac{1}{2}\boldsymbol{S} - \partial_{\mathbf{C}}\Psi\right] : \dot{\mathbf{C}} + [\eta - \partial_T \Psi]\dot{T} + [\mu - \partial_C \Psi]\dot{C} - \mathbf{j_R} \cdot \nabla_{\mathbf{X}}\mu - \frac{1}{T}\mathbf{q_R} \cdot \nabla_{\mathbf{X}} T \geq 0 \tag{24}$$

This inequality should hold for all values of $\mathbf{C}$, C, T, $\nabla_{\mathbf{X}}\mu$ and $\nabla_{\mathbf{X}} T$. Since there is a linear dependence on the temporal rates of deformation gradient, concentration and temperature, the terms between brackets must vanish, thus reaching the expressions for Eqs. (17e)-(17g). In addition to this, the expressions for the constraint on the fluid-flux inequality render

$$-\mathbf{q_R} \cdot \nabla_{\mathbf{X}} T \geq 0 \qquad \text{when} \quad \nabla_{\mathbf{X}} T \neq 0 \tag{25}$$

and the heat-flux inequality:

$$-\mathbf{j_R} \cdot \nabla_{\mathbf{X}}\mu \geq 0 \qquad \text{when} \quad \nabla_{\mathbf{X}}\mu \neq 0 \tag{26}$$

Further derivations can be done by considering the previous Legendre transformation carried out, where we reached the balance for the entropy:

$$\rho_0 \dot{\eta} T = R - \nabla_{\mathbf{X}} \cdot \mathbf{q}_{\mathbf{R}} - \mathbf{j}_{\mathbf{R}} \cdot \nabla_{\mathbf{X}} \mu \tag{27}$$

From here, the rate of entropy yields:

$$\rho_0 \dot{\eta} = \rho_0 [-\partial^2_{TT} \Psi \dot{T} - \frac{1}{2} \partial^2_{T\mathbf{C}} \Psi : \dot{\mathbf{C}} - \partial^2_{TC} \Psi \dot{C}] \tag{28}$$

The left-hand side of Eq. (27) may be expressed as

$$\rho_0 \dot{\eta} T = c_p \dot{T} - \rho_0 H \tag{29}$$

where the heat capacity c_p and the latent heat H are expressed as

$$c_p := -\rho_0 T \partial^2_{TT} \Psi; \qquad H = \frac{1}{2} T \partial^2_{T\mathbf{C}} \Psi : \dot{\mathbf{C}} + T \partial^2_{TC} \Psi \dot{C} = \frac{1}{2} T \mathbf{Z} : \dot{\mathbf{C}} + T Y \dot{C} \tag{30}$$

where $\mathbf{Z}$ and Y relate to the second-order tensor and the scalar term associated with the coupling of the motion and the mass transport in the Helmholtz free energy function, respectively. From here, the final expression for the transient heat equation reads:

$$c_p \dot{T} := \rho_0 H + R - \nabla_{\mathbf{X}} \cdot \mathbf{q}_{\mathbf{R}} - \mathbf{j}_{\mathbf{R}} \cdot \nabla_{\mathbf{X}} \mu \tag{31}$$

3.2. Time discrete mixed $\boldsymbol{u}-\mu$ potential and material model

The total potential model of the system can be divided into internal Π_{int} and external contributions Π_{ext}.

$$\Pi(\mathbf{u}, C, \mu, T; t) = \Pi_{\text{int}}(\mathbf{u}, C, \mu, T; t) - \Pi_{\text{ext}}(\mathbf{u}, C, \mu, T; t) \tag{32}$$

Complying with the formulation proposed by Miehe and coauthors [66] for Cahn-Hilliard diffusion-type problems, the proposed potential in Eq. (32) can be adjusted for a displacement-potential-density problem or gradient type-dissipative solids at a time interval $\Delta t = t_{n+1} - t_n$ in absence of external contributions as:

$$\Pi_{int}(\mathbf{C}, \mu, \nabla_{\mathbf{X}} \mu, C, T) = \Psi(\mathbf{C}, T) - \mu(C_{n+1} - C_n) - \Delta t \, \phi(\nabla_{\mathbf{X}} \mu, \mathbf{F}_n, C_n) \tag{33}$$

where ϕ is the convex dissipation potential. From here on, the subscript n refers to magnitudes of the previous increment. It is crucial to emphasize that the $\boldsymbol{u}-\mu$ problem is formulated without incorporating the dissipative components of the thermal problem. This approach is intentionally chosen to provide a variational foundation for the other two fields, thereby simplifying the implementation process. By excluding these dissipative terms, the derivatives of the mobility tensor naturally cancel out, as a result of the push-forward operation being applied at the preceding time step.

Since the proposed framework is dedicated for hydrogels, the attention is driven to materials with a quasi-incompressible behavior under loading at the instantaneous behavior. To account for this, they are considered to change their volume only due to swelling when absorbing solvents, since both the cross-linked polymer network and the solvent molecules are incompressible [40, 44]. Thus, this constraint is introduced as follows

$$J = 1 + \nu C \tag{34}$$

where ν refers to the volume of one solvent molecule. Considering the incremental character of the proposed model, this constraint is modified to:

$$J_{n+1} - J_n = \nu (C_{n+1} - C_n) \tag{35}$$

With the consideration of Eq. (35), the potential proposed in Eq. (33) can be postulated by reducing the set of arguments

$$\Pi_{int}(\mathbf{C}, p, \mathbb{p}, T) = \Psi(\mathbf{C}, T) - p(J_{n+1} - J_n) - \Delta t\, \phi(\mathbb{p}, \mathbf{F}_n, T) \tag{36}$$

where p is the scaled chemical potential, denoted in units of fluid pressure per mass. This magnitude and its gradient are introduced as follows:

$$p = \frac{\mu}{\nu}; \qquad \mathbb{p} = -\nabla_{\mathbf{x}} p \tag{37}$$

Expressing the approach on the current configuration, based on the formulation proposed by Flory and Rehner [67], we postulate the existence of a local free energy function Ψ, which has three contributions, one associated to the stretching of the polymer Ψ_{elas}, which reads

$$\Psi_{\text{elas}}(\mathbf{C}) = \frac{1}{2} N k_B T (I_1 - 3 - 2\log J) \tag{38}$$

another one related to the mixing of the polymer and solvent molecules Ψ_{mix} [68, 69]

$$\Psi_{\text{mix}}(\mathbf{C}, T) = \frac{k_B T}{\nu}\left[(J-1)\log\left(\frac{J-1}{J}\right) + \frac{\chi(T)(J-1)}{J}\right] \tag{39}$$

where I_1 is the first invariant of the left Cauchy-Green tensor that is defined as $I_1 := \text{tr}[\mathbf{C}]$, N is the number of chains segments per unit reference volume, T is the temperature, k_B is the Boltzmann constant and $\chi(T)$ refers to a material-specific and temperature-dependent interaction parameter. $\chi(T)$ is evaluated as the following expression proposed for LCST hydrogels in [44]:

$$\chi(T) = \frac{1}{2}(\chi_L + \chi_H) - \frac{1}{2}(\chi_L - \chi_H)\tanh\left(\frac{T - T_c}{\Delta}\right) \tag{40}$$

which is easily adopted to UCST hydrogels by changing the sign of the term with the hyperbolic tangent

$$\chi(T) = \frac{1}{2}(\chi_L + \chi_H) + \frac{1}{2}(\chi_L - \chi_H)\tanh\left(\frac{T - T_c}{\Delta}\right) \tag{41}$$

where χ_L and χ_H are the lower and upper limits of the parameter; T_c is the LCST/UCST value and Δ is the width of temperature range in the transition from both limits.

The final contribution of the energy is composed of the thermal contribution Ψ_{temp}, which follows a classical thermoelastic contribution

$$\Psi_{\text{temp}}(\mathbf{C}, T) = c_p\left[(T - T_0) - T\log\frac{T}{T_0}\right] - 3\kappa\alpha(T - T_0)\log J \tag{42}$$

where T_0 is the reference temperature, α stands for the coefficient for thermal expansion and κ is the bulk modulus of the gel.

The sum of these three contributions makes the expression for the local free energy function, for the last term in expression.

$$\Psi = \Psi_{\text{elas}} + \Psi_{\text{mix}} + \Psi_{\text{temp}} \tag{43}$$

Then, from Eq.(43), the Cauchy stress tensor $\boldsymbol{\sigma}$ can be computed as follows:

$$\mathbf{S} := 2\frac{\partial \Psi(\mathbf{C})}{\partial \mathbf{C}} - pJ\mathbf{C}^{-1} = Nk_BT(\mathbf{1}-\mathbf{C}^{-1}) + \left[\frac{k_BT}{\nu}\left[\log\left(\frac{J-1}{J}\right)+\frac{1}{J}+\frac{\chi}{J^2}\right]-3\kappa\alpha(T-T_0)-p\right]J\mathbf{C}^{-1} \quad (44)$$

In order to implement the present model into the general purpose FE software, `ABAQUS`, via the `UEL` subroutine, the local tangent operator $\mathbb{C}$ is required to compute the Jacobians. $\mathbb{C}$ can be obtained directly from the derivation of Eq. (44):

$$\begin{aligned}\mathbb{C} = 2\frac{\partial \mathbf{S}}{\partial \mathbf{C}} =& 2J\left[Nk_BT - \frac{k_BT}{\nu}\left[\log\left(\frac{J-1}{J}\right)+\frac{1}{J}+\frac{\chi}{J^2}\right]+3\kappa\alpha(T-T_0)+p\right]\mathbf{I}^{\mathrm{sym}}_{\mathbf{C}} \\ &- \left[\frac{k_BT}{\nu}\left[\frac{\chi}{J^2}-\log\left(\frac{J-1}{J}\right)-\frac{1}{J-1}\right]+3\kappa\alpha(T-T_0)+p\right]J\mathbf{C}^{-1}\otimes\mathbf{C}^{-1}\end{aligned} \quad (45)$$

where $\mathbf{I}^{\mathrm{sym}}_{\mathbf{C}}$ is a fourth-order tensor that has the following expression: $\mathbf{I}^{\mathrm{sym}}_{\mathbf{C}} := [\mathbf{C}^{-1}\overline{\otimes}\mathbf{C}^{-1}+\mathbf{C}^{-1}\underline{\otimes}\mathbf{C}^{-1}]/2 = [C^{-1}_{ik}C^{-1}_{jl}+C^{-1}_{il}C^{-1}_{jk}]/2$, which employs the non-standard dyadic products.

For the mass diffussion problem, a dissipation function ϕ is postulated

$$\phi(\mathbb{p},T) = \frac{1}{2}(J_n-1)\frac{D\nu}{k_BT}|\mathbb{p}|^2 \quad (46)$$

where D is the diffusivity coefficient and $|\bullet|$ is the absolute value operator. From this expression, one can derive it to obtain the flux vector referred to the current configuration $\mathbf{j} = J_n^{-1}\frac{\partial\phi}{\partial\mathbb{p}}$, that reads as

$$\mathbf{j} = \frac{(J_n-1)}{J_n}\frac{D\nu}{k_BT}\mathbb{p} \quad (47)$$

and then, by doing the pull-back operation, we obtain the nominal mass flux $\mathbf{j_R}$

$$\mathbf{j_R} = \mathbf{F}_n^{-\mathrm{T}}(J_n-1)\frac{D\nu}{k_BT}\mathbf{F}_n^{-\mathrm{T}}\cdot\mathbb{P} \quad (48)$$

where $\mathbb{P} = -\nabla_{\mathbf{X}}p$. Keep in mind that the mixing potential (Eq. (46)) is due to the incremental changes of the species concentration with respect to the previous increment. This justifies the appearance of $\mathbf{F_n}$ in Eq. (48).

At last, to account for the thermal problem, the entropy η is obtained from the derivation of the temperature on Eq. (42).

$$\begin{aligned}\eta_R = -\frac{\partial\Psi}{\partial T} =& 3\kappa\alpha\log J + c_p\log\frac{T}{T_0} - \frac{1}{2}Nk_B(I_1-3-2\log J) \\ &- \frac{k_B}{\nu}\left[(J-1)\log\left(\frac{J-1}{J}\right)+\frac{\chi(T)(J-1)}{J}\right] - \frac{(J-1)k_BT}{J\nu}\frac{\partial\chi(T)}{\partial T}\end{aligned} \quad (49)$$

Therefore, from this expression, the latent heat H reads:

$$H = \frac{1}{2}T\partial^2_{T\mathbf{C}}\Psi:\dot{\mathbf{C}} + T\partial^2_{TC}\Psi:\dot{C} = \frac{1}{2}\mathbf{Z}:\dot{\mathbf{C}} \quad (50)$$

Obtained from Eq. (49), only the deformation problem contributes to the latent heat, therefore $Y = 0$ and $\mathbf{Z}$ (i.e., the structural heating for hydrogels) is easily obtained by deriving Eq. (49) with respect to the temperature (see Eq. (55c)). To conclude with the temperature part, we define the expression for the current heat flux which reads

$$\mathbf{q} = -\mathbf{k} \cdot \nabla_{\mathbf{x}} T \tag{51}$$

and by performing the pullback operation we reach the nominal flux $\mathbf{q_R}$.

$$\mathbf{q_R} = -J\mathbf{F}^{-1} \cdot \mathbf{k} \cdot \mathbf{F}^{-\mathrm{T}} \cdot \nabla_{\mathbf{X}} T = -\mathbf{K} \cdot \nabla_{\mathbf{X}} T \tag{52}$$

It is a common practice to identify an initial preswollen state due to Ψ_{mix} being singular for $J = 1$, i.e., in the dry state [41]. Therefore, there is a huge convenience in establishing a pre-swollen state in chemo-mechanical equilibrium as a referential state [70], which results in the decomposition for the deformation gradient as

$$\mathbf{F}^* = \mathbf{F} \cdot \mathbf{F_0} \tag{53}$$

and the expression of Π_{int} reads:

$$\Pi_{\text{int}}(\mathbf{C}^*, p, \mathbb{p}, \mathbf{F_0}, \mathbf{F_n}, T) = \frac{1}{J_0}\Psi(\mathbf{C}^*, T) - p(J_{n+1} - J_n) - \frac{1}{J_0}\Delta t\, \phi(\mathbb{p}, \mathbf{F_0}, \mathbf{F_n}, T) \tag{54}$$

resulting this in an alternative representation for the stress, the mass flux and the displacement-temperature coupling tensor

$$\mathbf{S} := \frac{Nk_BT}{J_0}(J_0^{2/3}\mathbf{1} - \mathbf{C}^{-1}) + \left[\frac{k_BT}{\nu}\left[\log\left(\frac{JJ_0 - 1}{JJ_0}\right) + \frac{1}{JJ_0} + \frac{\chi(T)}{J^2J_0^2}\right] - \frac{3\kappa\alpha(T - T_0)}{J_0} - p\right] J\mathbf{C}^{-1} \tag{55a}$$

$$\mathbf{j_R} = \frac{J_nJ_0 - 1}{J_0^2}\frac{D\nu}{k_BT}\mathbf{F}_n^{-\mathrm{T}} \cdot \mathbf{F}_n^{-\mathrm{T}} \cdot \mathbb{P} = m\mathbf{F}_n^{-\mathrm{T}} \cdot \mathbf{F}_n^{-\mathrm{T}} \cdot \mathbb{P} \tag{55b}$$

$$\mathbf{Z} = \frac{Nk_B}{J_0}(J_0^{2/3}\mathbf{1} - \mathbf{C}^{-1}) + \frac{k_BJ}{\nu}\left[\log\left(\frac{J - 1}{J}\right) + \frac{1}{J} + \frac{\chi(T)}{J^2}\right]\mathbf{C}^{-1} \pm \frac{k_BTJ}{\nu J^2J_0^2}\frac{\chi_L - \chi_H}{2\Delta\cosh^2\left(\frac{T - T_c}{\delta}\right)}\mathbf{C}^{-1} - 3\kappa\alpha\mathbf{1} \tag{55c}$$

with $m = \frac{J_nJ_0 - 1}{J_0^2}\frac{D\nu}{k_BT}$. The expression for $\mathbf{Z}$ depends on whether it is a UCST or LCST hydrogel.

3.3. Derivation of the formulation

In this subsection, the basis of the mixed coupled displacement-pressure-temperature problem is outlined. First, for displacement and pressure equations, the total potential of the system can be expressed in the reference position of the arbitrary body by considering the dependence on the primary variables as follows

$$\Pi(\mathbf{u}, p, T, t) = \int_{\Omega_0} \Pi_{\text{int}}(\mathbf{u}, p, T, t)\mathrm{d}V - \Pi_{\text{ext}}(\mathbf{u}, p, T, t) \tag{56}$$

while for the temperature expression, the derivations are obtained from Eq. (31), which is obtained after applying the Legendre transformation. The reason behind dedicating special attention to the thermal component is detailed in [65]. This shows that our formulation is partially variational, as only the contributions for displacement and pressure are derived from the potential defined in Section 3.2.

To solve the problem, consider the variation of primary fields $(\mathbf{u}, p, T)$ as $(\delta\mathbf{u}, \delta p, \delta T)$ in the appropriate spaces $(\mathfrak{V}^u, \mathfrak{V}^p, \mathfrak{V}^T)$. It is worth noting that $\mathfrak{V}^u = \left\{\delta\mathbf{u} \in [H^1(\Omega_0)] : \delta\mathbf{u} = \mathbf{0} \text{ on } \partial\Omega_{0,\mathbf{u}}\right\}$ is the space of

admissible displacement variations, $\mathfrak{V}^p = \{\delta p \in H^1(\Omega_0) : -\mathbf{j_R} \cdot \nabla_{\mathbf{X}} \nu \delta p \geq 0 \text{ on } \partial\Omega_{0,j}\}$ is the field space of the admissible pressure and $\mathfrak{V}^T = \{\delta T \in H^1(\Omega_0) : -\mathbf{q_R} \cdot \nabla_{\mathbf{X}} \delta T \geq 0 \text{ on } \partial\Omega_{0,q}\}$ denotes the admissible test functions for the temperature field.

The problem is first ruled via the linear momentum equilibrium for the mechanical part, defined in Eq. (14) and for the dissipation function for the mass transport, postulated in Eq. (46). By combining the first two terms, we define the expression for total internal potential postulated in Eq. (33), and from here, we define the weak form of both equations, which stand for the most convenient setting to write the corresponding numerical approximation based on FEM based on the standard Galerkin procedure:

$$\mathrm{D}\,\Pi(\delta\mathbf{u}) = \int_{\Omega_0} \Big[\mathrm{D}\,\Psi(\delta\mathbf{u}) - p\mathrm{D}\,J[\delta\mathbf{u}]\Big]\mathrm{d}V - \mathrm{D}\,\Pi_{\text{ext}}(\delta\mathbf{u}) = 0, \quad \forall\delta\mathbf{u} \tag{57a}$$

$$\mathrm{D}\,\Pi(\delta p) = \int_{\Omega_0} \Big[-(J - J_n)\mathrm{D}\,p(\delta p) - \Delta t \mathrm{D}\,\phi(\delta p)\Big]\mathrm{d}V - \mathrm{D}\,\Pi_{\text{ext}}(\delta p) = 0, \quad \forall\delta p \tag{57b}$$

The weak definition of the thermal contribution is obtained from the energy balance in entropy form for the thermal part, defined in Eq. (31), which reads

$$\int_{\Omega_0} \Big[c_p \mathrm{D}\dot{T}(\delta T) + \mathrm{D}\,\nabla\cdot\mathbf{q_R}(\delta T) - \mathrm{D}T(\delta T)\mathbf{Z} : \dot{\mathbf{C}} - m\nu\mathrm{D}\nabla p(\delta T)\Big]\mathrm{d}V - \mathrm{D}\,\Pi_{\text{ext}}(\delta T) = 0, \quad \forall\delta T \tag{58}$$

where the operator $\mathrm{D}\,F(\delta\bullet)$ denotes the Gateaux derivative which reads as:

$$\mathrm{D}\,F(\delta\bullet) = \frac{\partial}{\partial\eta} F(\bullet + \eta\delta\bullet)|_{\eta=0} \tag{59}$$

By introducing the second Piola-Kirchhoff stress $\mathbf{S}$, the nominal heat flux $\mathbf{q_R}$ and the nominal mass flux $\mathbf{j_R}$, it is obtained the weak form of the coupled displacement-pressure-temperature problem for large deformation solids with diffusion problems:

$$\int_{\Omega_0} \Big[\mathbf{S} : \mathbf{E}(\delta\mathbf{u})\Big]\,\mathrm{d}V - \mathrm{D}\,\Pi_{\text{ext}}(\delta\mathbf{u}) = 0,\ \forall\delta\mathbf{u} \tag{60a}$$

$$\int_{\Omega_0} \Big[-(J - J_n)\delta p + \Delta t\,\mathbf{j_R}\cdot\nabla_{\mathbf{X}} p(\delta p)\Big]\mathrm{d}V - \mathrm{D}\,\Pi_{\text{ext}}(\delta p) = 0,\ \forall\delta p \tag{60b}$$

$$\int_{\Omega_0} \Big[c_p\dot{T}(\delta T) - \frac{1}{2}T\mathbf{Z} : \dot{\mathbf{C}}(\delta T) + J\nabla_{\mathbf{X}} T\cdot\mathbf{K}\cdot\nabla_{\mathbf{X}}(\delta T) - \mathbf{j_R}(\delta T)\cdot\nabla_{\mathbf{X}} p\Big]\mathrm{d}V - \mathrm{D}\,\Pi_{\text{ext}}(\delta T) = 0,\ \forall\delta T \tag{60c}$$

4. Finite Element formulation and implementation details

4.1. Discretisation scheme

Being the domain discretized into finite elements, for which the displacement, scaled chemical potential and the temperature are approximated by Galerkin's method as it follows

$$\mathbf{u} = \sum_{i=1}^{n} \mathbf{N_d}\cdot\mathbf{d}, \quad p = \sum_{i=1}^{m} \mathbf{N_p}\cdot\hat{\mathbf{p}}, \quad T = \sum_{i=1}^{m} \mathbf{N_T}\cdot\hat{\mathbf{T}} \tag{61}$$

where $\mathbf{d}$ represents the nodal displacement vector; $\hat{\mathbf{p}}$ is the nodal values of the pressure variable and $\hat{\mathbf{T}}$ stands for the nodal interpolation of the temperature. In order to satisfy the Babuska-Brezzi conditions [71] and

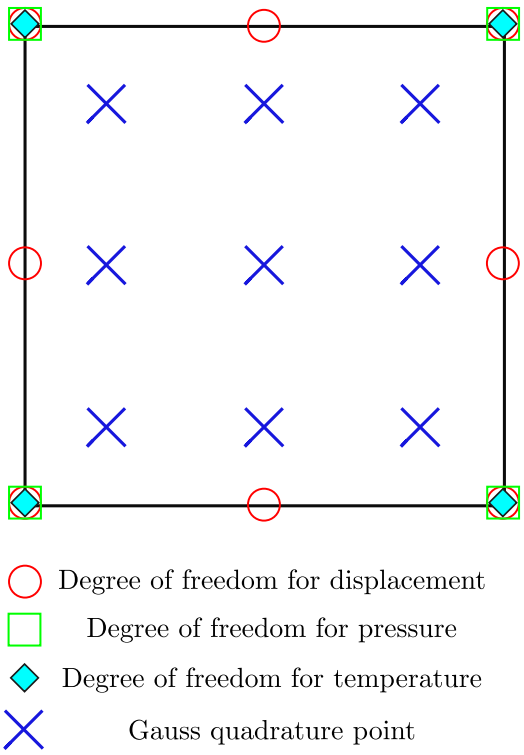

Figure 3: 2-D illustration of a **u**-p-T mixed finite element, displaying the degrees of freedom and the Gauss quadrature points. 8-node quadratic element is used for the displacement while 4-node bilinear quadrilateral elements are utilized for pressure and temperature.

avoid poor numerical performance, we employ a Taylor-Hood element discretization, where the displacement shape functions are taken to correspond to a biquadratic 8-node serendipity element (20-node in 3-D), while for temperature and scaled chemical potential we employ bilinear shape functions for a 4-node quadrilateral element (8-node in 3-D). A schematic illustration of the discretization for two dimensions is provided in Fig. 3.

The material and spatial gradients of the shape functions $\mathbf{N}$ can be read as

$$\nabla_{\mathbf{X}}\mathbf{N} = \mathbf{J_e}^{-\mathrm{T}} \cdot \nabla_{\boldsymbol{\xi}}\mathbf{N}(\boldsymbol{\xi}), \qquad \nabla_{\mathbf{x}}\mathbf{N} = \mathbf{j_e}^{-\mathrm{T}} \cdot \nabla_{\boldsymbol{\xi}}\mathbf{N}(\boldsymbol{\xi}) \tag{62}$$

with $\boldsymbol{\xi}$ referring to the parametric coordinate system with coordinates $\boldsymbol{\xi} = \{\xi, \eta, \zeta\}$; and $\mathbf{J_e}$ and $\mathbf{j_e}$ as the material and spatial Jacobians of the isoparametric transformation, which allow the computation of the deformation gradient $\mathbf{F}$ as follows:

$$\mathbf{F} = \mathbf{j_e} \cdot \mathbf{J_e}^{-1} \qquad \text{with } J_e = \det[\mathbf{F}] = \frac{\det[\mathbf{j_e}]}{\det[\mathbf{J_e}]} \tag{63}$$

With the previous definitions at hand, the corresponding material gradient quantities can be discretized as, for a material description,

$$\nabla_{\mathbf{X}}\delta\mathbf{u} \approx \delta\mathbf{d} \otimes \nabla_{\mathbf{X}}\mathbf{N_d}, \qquad \nabla_{\mathbf{X}}\delta p \approx \delta\hat{\boldsymbol{p}} \otimes \nabla_{\mathbf{X}}\mathbf{N_p}, \qquad \nabla_{\mathbf{X}}\delta T \approx \delta\hat{\boldsymbol{T}} \otimes \nabla_{\mathbf{X}}\mathbf{N_T} \tag{64}$$

where $[\delta\mathbf{d}, \delta\hat{\boldsymbol{p}}, \delta\hat{\boldsymbol{T}}]$ are the nodal test functions.

4.2. Consistent linearization of the coupled displacement-pressure-temperature problem

Considering a finite time increment $\Delta t := t_{n+1} - t_n > 0$, where all the DOFs at t_n are assumed to be known. The target is to obtain the independent variables at the time t^k_{n+1} for the k-th iteration. To do so, we solve the coupled problem through the use of the incremental and iterative solvers. This requires the computation by the consistent lineralization of the previous residual equations in the sense of the Gateaux directional derivative. Within this frame, the temporal variation of the displacement, pressure and temperature reads:

$$\dot{\mathbf{d}} = \frac{\mathbf{d}_{n+1} - \mathbf{d}_n}{\Delta t}; \qquad \dot{\hat{p}} = \frac{\hat{p}_{n+1} - \hat{p}_n}{\Delta t}; \qquad \dot{\hat{T}} = \frac{\hat{T}_{n+1} - \hat{T}_n}{\Delta t} \tag{65}$$

The point of departure for the finite element formulation of the displacement-pressure recalls the formalism defined in Eqs.(60a)-(60c), defining a coupled problem. The insertion of the interpolation scheme for $\mathbf{u}$, p and T leads to a discrete version of the residual forms denoted by $\mathbf{R}^{\mathbf{d}}$, $\mathbf{R}^{\hat{p}}$ and $\mathbf{R}^{\hat{T}}$ that are defined as:

$$\mathbf{R}^{\mathbf{d}}(\mathbf{d}, \hat{p}, \hat{T}) = (\delta\mathbf{d})^{\mathrm{T}} \left[\int_{\Omega_0} \nabla_{\mathbf{X}} \mathbf{N}^{\mathrm{T}}_{\mathbf{d}} \cdot \mathbf{S} \, \mathrm{d}V - \int_{\Omega_0} \mathbf{N}^{\mathrm{T}}_{\mathbf{d}} \cdot \overline{\mathbf{F}}^{V} \, \mathrm{d}V - \int_{\partial\Omega_0} \mathbf{N}^{\mathrm{T}}_{\mathbf{d}} \cdot \overline{\mathbf{T}} \, \mathrm{d}\partial V \right] = 0 \tag{66a}$$

$$\mathbf{R}^{\hat{p}}(\mathbf{d}, \hat{p}, \hat{T}) = (\delta\hat{\boldsymbol{p}})^{\mathrm{T}} \left[\int_{\Omega_0} -\mathbf{N}^{\mathrm{T}}_{\mathbf{p}} (J - J_n) \, \mathrm{d}V + \int_{\Omega_0} \frac{\Delta t}{J_0} \, \mathbf{F}_n^{-\mathrm{T}} \cdot \nabla_{\mathbf{X}} \mathbf{N}^{\mathrm{T}}_{\mathbf{p}} \cdot \mathbf{j}_{\mathbf{R}} \, \mathrm{d}V \right] = 0 \tag{66b}$$

$$\begin{aligned} \mathbf{R}^{\hat{T}}(\mathbf{d}, \hat{p}, \hat{T}) = (\delta\hat{\boldsymbol{T}})^{\mathrm{T}} \Bigg[& \int_{\Omega_0} \mathbf{N}^{\mathrm{T}}_{\mathbf{T}} c_p \left(\frac{T - T_n}{\Delta t} \right) \mathrm{d}V + \int_{\Omega_0} \nabla_{\mathbf{X}} \mathbf{N}^{\mathrm{T}}_{\mathbf{T}} \cdot \mathbf{K} \cdot \nabla_{\mathbf{X}} T \mathrm{d}V \\ & - \int_{\Omega_0} \frac{\mathbf{N}^{\mathrm{T}}_{\mathbf{T}}}{2} (\mathbf{Z}^{\mathrm{T}} : \dot{\mathbf{C}}) \, T \mathrm{d}V + \int_{\Omega_0} \mathbf{N}^{\mathrm{T}}_{\mathbf{T}} \cdot \mathbf{j}_{\mathbf{R}} \cdot \nabla_{\mathbf{X}} p \mathrm{d}V \Bigg] = 0 \end{aligned} \tag{66c}$$

For the application of Newton-type solution algorithms for the iterative solution of the boundary value problem, the linearization of the weak form has been computed, leading to the following linearised system of equations that is solved by the global N-R monolithic scheme

$$\begin{bmatrix} \mathbf{K}^{\mathbf{dd}} & \mathbf{K}^{\mathbf{d}\hat{p}} & \mathbf{K}^{\mathbf{d}\hat{T}} \\ \mathbf{K}^{p\mathbf{d}} & \mathbf{K}^{\hat{p}\hat{p}} & \mathbf{K}^{\hat{p}\hat{T}} \\ \mathbf{K}^{\hat{T}\mathbf{d}} & \mathbf{K}^{\hat{T}\hat{p}} & \mathbf{K}^{\hat{T}\hat{T}} \end{bmatrix} \begin{bmatrix} \Delta\mathbf{d} \\ \Delta\hat{\mathbf{p}} \\ \Delta\hat{\mathbf{T}} \end{bmatrix} = - \begin{bmatrix} \mathbf{R}^{\mathbf{d}} \\ \mathbf{R}^{\hat{p}} \\ \mathbf{R}^{\hat{T}} \end{bmatrix} \tag{67}$$

being the tangent operators of the proposed finite element for the fully-coupled implicit solution scheme derived from the residual operators as

$$\mathbf{K^{dd}} = \frac{\partial \mathbf{R}^d}{\partial \mathbf{u}} = \int_{\Omega_0} \nabla_{\mathbf{X}} \mathbf{N}_{\mathbf{d}}^{\mathrm{T}} \cdot \mathbb{C} \cdot \nabla_{\mathbf{X}} \mathbf{N}_{\mathbf{d}} \, \mathrm{d}V + \int_{\Omega_0} \left[\nabla_{\mathbf{X}} \mathbf{N}_{\mathbf{d}}^{\mathrm{T}} \cdot \mathbf{S} \cdot \nabla_{\mathbf{X}} \mathbf{N}_{\mathbf{d}} \right] \cdot \mathbf{1} \, \mathrm{d}V \tag{68a}$$

$$\mathbf{K^{d\hat{p}}} = (\mathbf{K^{\hat{p}d}})^{\mathrm{T}} = \frac{\partial \mathbf{R}^d}{\partial p} = -\int_{\Omega_0} J \, \nabla_{\mathbf{X}} \mathbf{N}_{\mathbf{d}}^{\mathrm{T}} \cdot \mathbf{C^{-1}} \cdot \mathbf{N_p} \, \mathrm{d}V \tag{68b}$$

$$\mathbf{K^{d\hat{T}}} = \frac{\partial \mathbf{R^d}}{\partial T} = \int_{\Omega_0} \nabla_{\mathbf{X}} \mathbf{N}_{\mathbf{d}}^{\mathrm{T}} \cdot \mathbf{Z} \cdot \mathbf{N_T} \, \mathrm{d}V \tag{68c}$$

$$\mathbf{K}^{\hat{p}\hat{p}} = \frac{\partial \mathbf{R}^{\hat{p}}}{\partial p} = -\int_{\Omega_0} \frac{\Delta t \; m \; J_n}{J_0} \, \mathbf{F_n}^{-\mathrm{T}} \cdot \nabla_{\mathbf{X}} \mathbf{N}_{\mathbf{p}}^{\mathrm{T}} \cdot \mathbf{F_n^{-1}} \cdot \nabla_{\mathbf{X}} \mathbf{N_p} \, \mathrm{d}V \tag{68d}$$

$$\mathbf{K}^{\hat{p}\hat{T}} = \frac{\partial \mathbf{R}^{\hat{p}}}{\partial T} = -\int_{\Omega_0} \frac{\Delta t}{T J_0} \, \mathbf{F_n}^{-\mathrm{T}} \cdot \nabla_{\mathbf{X}} \mathbf{N}_{\mathbf{p}}^{\mathrm{T}} \cdot \mathbf{j_R} \cdot \mathbf{N_T} \, \mathrm{d}V \tag{68e}$$

$$\mathbf{K}^{\hat{T}\mathbf{d}} = \frac{\partial \mathbf{R}^{\hat{T}}}{\partial \mathbf{d}} = -\int_{\Omega_0} \frac{T}{\Delta t} \mathbf{N}_{\mathbf{T}}^{\mathrm{T}} \cdot \mathbf{Z^T} \cdot \nabla_{\mathbf{X}} \mathbf{N_d} \, \mathrm{d}V \tag{68f}$$

$$\mathbf{K}^{\hat{T}\hat{p}} = \frac{\partial \mathbf{R}^{\hat{T}}}{\partial \hat{p}} = \int_{\Omega_0} m \mathbf{N}_{\mathbf{T}}^{\mathrm{T}} \cdot \mathbf{j_R} \cdot \mathbf{F_n}^{-\mathrm{T}} \cdot \nabla_{\mathbf{X}} \mathbf{N_p} \, \mathrm{d}V \tag{68g}$$

$$\begin{aligned} \mathbf{K}^{\hat{T}\hat{T}} = \frac{\partial \mathbf{R}^{\hat{T}}}{\partial T} &= \int_{\Omega_0} \mathbf{N}_{\mathbf{T}}^{\mathrm{T}} \frac{c_p}{\Delta t} \cdot \mathbf{N_T} \; - \int_{\Omega_0} \mathbf{N}_{\mathbf{T}}^{\mathrm{T}} \frac{(\mathbf{Z}^{\mathrm{T}} : \dot{\mathbf{C}})}{2} \cdot \; \mathbf{N_T} \, \mathrm{d}V \\ &+ \int_{\Omega_0} \nabla_{\mathbf{X}} \mathbf{N}_{\mathbf{T}}^{\mathrm{T}} \cdot \mathbf{K} \cdot \mathbf{F}^{-\mathrm{T}} \cdot \nabla_{\mathbf{X}} \mathbf{N_T} \, \mathrm{d}V - \int_{\Omega_0} \mathbf{N}_{\mathbf{T}}^{\mathrm{T}} \cdot \frac{\mathbf{j_R} \cdot \nabla_{\mathbf{X}} p}{T} \cdot \mathbf{N_T} \, \mathrm{d}V \end{aligned} \tag{68h}$$

The `Q2Q1Q1` fully-coupled element that we are presenting is programmed via an `UEL` user element subroutine from the FE commercial package `ABAQUS`. The solution scheme employed for the aforementioned simulation is an incremental-iterative Newton-Raphson and the performance of the presented formulation will be put into test in the next Section via the conduction of various numerical examples concerning several applications of thermoresponsive hydrogels.

5. Numerical experiments

The organization within this Section is based on the evaluation of distinct numerical examples and the corresponding outcomes derived from each of them. Section 5.1 presents a benchmark example featuring a bidimensional square LCST hydrogel. This initial test aims to test the functionality of the `Q2Q1Q1` formulation. To achieve this objective, the sample is subject to free transient swelling and subsequently, to deswelling caused by a temperature increase in Section 5.1.1. Subsequently, this specimen is used in addressing a couple of distinctive aspects within our study. First, in Section 5.1.2, we delve into the dependence of the mesh refinement on the increment of the diffusion length. For this, our analysis analyzes the oscillations in pressure during the initial phases of the swelling test for different mesh discretizations. Then, in Section 5.1.3, the influence of the mass flux and the hyperelastic stretching in the temperature field is addressed for this specimen.

Aiming for more complex problems, the compression behavior of UCST hydrogel sphere-like specimens that are already in a swollen state is evaluated for different initial temperatures in Section 5.2. Eventually, in Section 5.3, the seminal experiments of Oh et al. [63] concerning the effect of cross-linking and temperature in the swelling ratio of *PNIPAAm* hydrogels are replicated with the modelling numerical framework.

5.1. Benchmark problem: 2-D square LCST hydrogel

5.1.1. Verification: free swelling and thermal deswelling

The first of the experiments consists of a validation example adopted for the experiment from Sec. 10.4 in the work by Chester and Anand [44]. In the light of this, it is modelled a 2-D plane-strain square brick

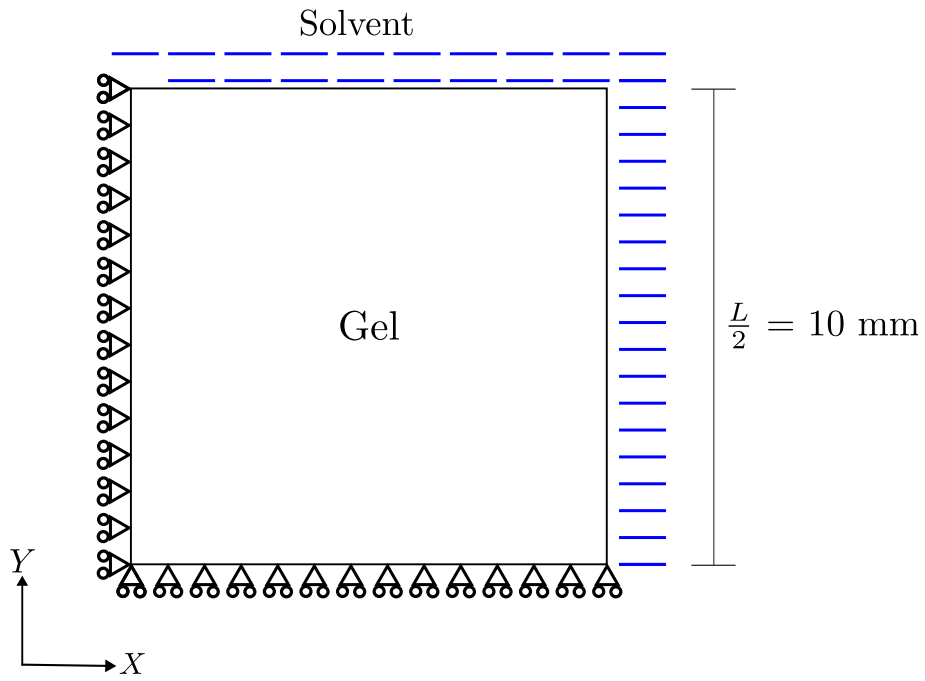

Figure 4: Configuration for the 2-D free swelling and thermal deswelling problem. Symmetry conditions are considered on the planes X and Y.

Table 1: Material properties employed for the isothermal square under free transient swelling and thermal-deswelling conditions.

$Nk_BT = \mu$ (MPa)	$N\nu$	T_c (K)	$\chi_L \approx \chi$	D (mm^2/s)	λ_0
0.4	0.01	320	0.1	5×10^{-3}	1.001

of $L = 20$ mm with 1,600 `Q2Q1Q1` elements, displayed in Fig. 4. The hydrogel is subject to the following initial boundary conditions (BCs):

- Concerning mechanical BCs, symmetry conditions are considered on the planes X and Y (see Fig. 4). Therefore, in the FE commercial package `ABAQUS` is modelled the quarter of the problem.
- Concerning mass flux BCs, initial condition for the pressure with p_0 for the whole domain in a stress-free equilibrium state is $p_0 = -188.86$ MPa with the fixed edges prescribed to a zero fluid flux.
- Concerning thermal BCs, the entire body is prescribed to a temperature of $T_0 = 298$ K under isothermal conditions (i.e., no external flux, $\mathbf{Z} = 0$), this means that the hydrogel is below the LCST temperature, therefore, according to Eq. (40), we can approximate $\chi_L \approx \chi$.

The material properties employed are represented in Tab. 1 and the main goal is to display the functionality of the proposed `Q2Q1Q1` formulation. Such demonstration is made for a free swelling state and subsequent deswelling caused by a temperature gradient. To perform this task, the test is comprised of the following stages:

- The first stage consists of a pressure decrease at the edges that are in contact with the solvent. This is performed via definition of a linear ramp in $t = 300$ s from p_0 to 0 MPa with a fixed time increment of $\Delta t = 3$ s. The motivation behind the choice of such time conditions is discussed in detail in Section 5.1.2.

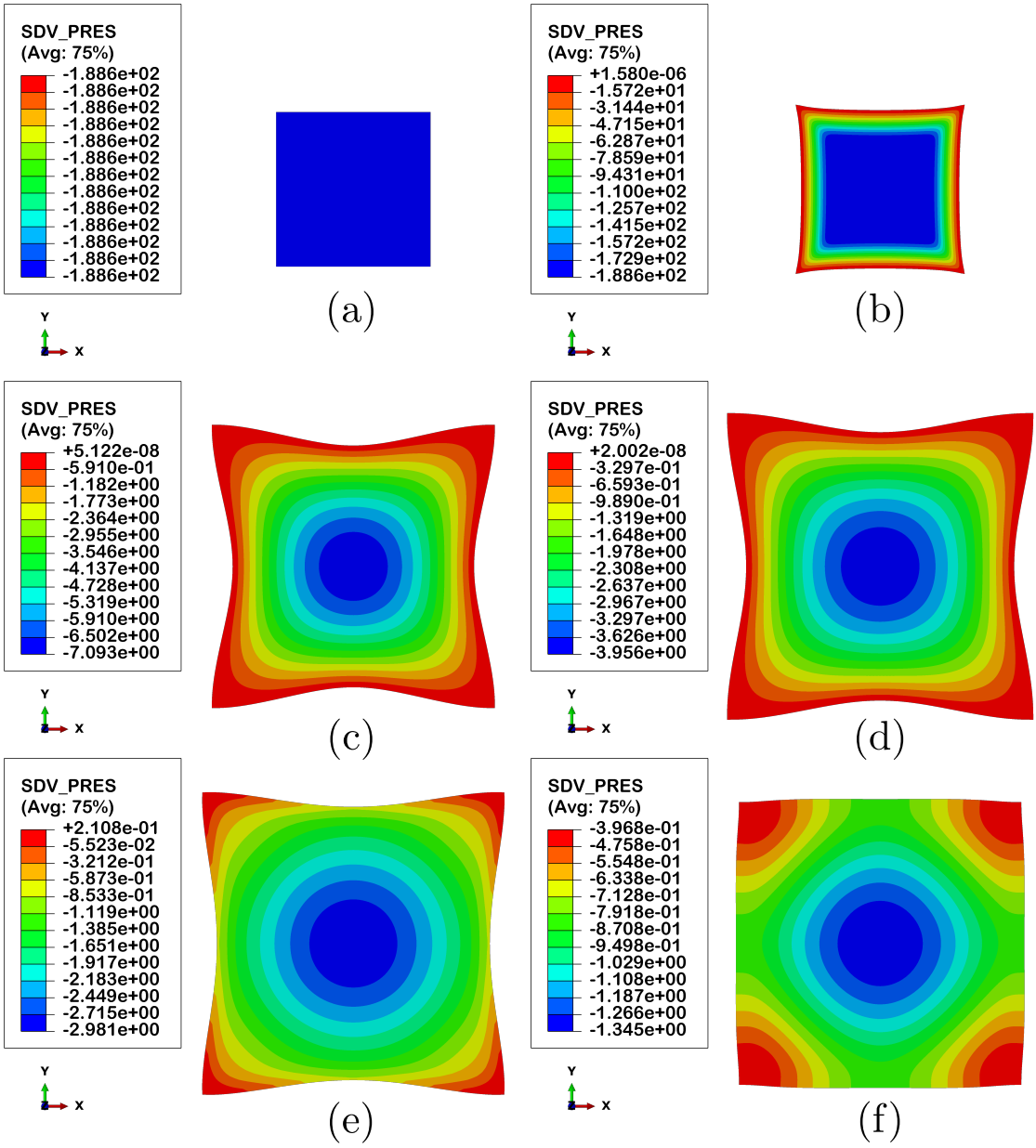

Figure 5: Steps of the swelling-deswelling process: states for (a) 0 s, (b) 300 s, (c) 12 h, (d) 24h, (e) 33h and (f) 49h. Represented within this plots is the solvent pressure p.

- Subsequently, the solid is subject to free transient swelling for 24 h.
- Then, when the model has swollen for such time, simulating a heating of the solvent, the edges in contact with it are prescribed for a linear ramp in temperature from T_0 to 333 K in 1 h, thus meaning that the hydrogel will overpass the LCST, reducing its swelling rate considerably.
- This last temperature is held for another 24 h to analyze properly how the hydrogel will be compressed under this thermal conditions.

Figs. 5(a)-5(f) depict the contour of the hydrostatic pressure, p, plotted on the deformed solid after

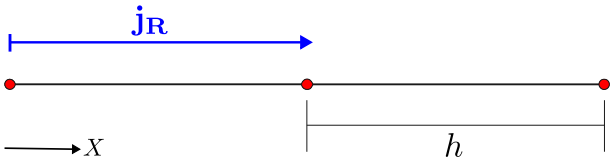

Figure 6: 1-D representation of the diffusion length problem.

different times: (a) 0 s; (b) 300 s; (c) 12 h; (d) 24 h; (e) 25 h; (f) 49 h. In summary, the whole evolution of the square during the test can be observed. Fig. 5(a) shows the application of the initial p_0 conditions, while Fig. 5(b) exhibits the results of the decrease of the pressure in the edges in contact with the solvent. Figs. 5(c)-5(d) exhibit the swollen body at the middle and at the end of the swelling step; and we can relate that the sample loses its square shape due to the fluid flux that is coming from both edges in contact with the solvent to the center of the sample. We can see from Figs. 5(b)-5(c) that the specimen grows more than from Figs. 5(c)-5(d), due to the major difference in mass flux that is on the former state. Subsequently, the results from thermal deswelling are observed in the last pair of images, Figs. 5(e)-5(f). Both images exhibit that once the LCST of $T_c = 320$ K has been surpassed, there is a decrease of size in the swollen state, approaching again the initial square configuration of the body. The results that we have displayed in this Section match qualitatively with those presented in the aforementioned paper of Chester and Anand [44]. However, some remarks need to be addressed regarding the presented framework, which are being covered in the forthcoming subsections.

5.1.2. Study of diffusion length at instantaneous loading state

Next, we investigate the observed oscillations that might arise at the instantaneous state once heat and mass flux boundary conditions are applied requiring a limit on the element size, informed from the diffusion length. Specifically, for smaller diffusivity coefficients D, as the diffusion length is decreasing, the mesh size is required to be finer in order to capture the transport problem.

Represented for a 1-D configuration in Fig. 6, we plot two elements with a size h which are experiencing mass diffusion under a referential flux $\mathbf{j_R}$. The problem states that in order to have a smooth transport problem, for an increment Δt, the flux should be fast enough to diffuse from at least one element of the mesh, meaning that the element size should be refined according to this. From here, we define an empirical rule $h \leq \sqrt{D\Delta t}$ to establish the minimum discretization that is required to model this. The failure to meet this condition causes oscillations in the pressure field that leads to convergence issues for the loading step.

To test the mesh dependence, various discretizations of the 2-D square block disposed to free swelling are simulated, with the properties plotted in Tab. 1. The main target is to assess the pressure oscillations of the specimen in the step for the unloading pressure linear ramp in the edges of the hydrogel exposed to the solvent from p_0 to 0 MPa. Adopting a final time of $t_f = 50$ s with a fixed time increment of $\Delta t = 0.5$ s, we obtain from the empirical condition that the maximum element size required to model the hydrogel pre-swelling step is $h = 0.05$ mm. It is important to highlight that now we consider the full chemo-thermomechanical model, i.e., $\mathbf{Z} \neq 0$, this means that heat sources are considered. However, as no special thermal BCs are added, we do not address the thermal particularities, leaving that for the following Section.

Displaying the pressure isocontour for the first step of the unloading step in Fig. 7, it can be identified for the first maps that when the boundaries of the specimen are put in contact with the solvent, the pressure gradient in that area becomes irregular due to oscillations that are happening within this magnitude. These are due to the diffusion length problem that we are addressing in this section, since the aforementioned condition is not fulfilled. It is observed when the specimen is refined, this transition becomes less rough, leading to a total stable sample for Fig. 7(d), when such criterion is met. A quantitative approach of this phenomenon can be observed in Fig. 8, where we plot the evolution of the pressure from a vertical path in $x = L - h$ mm; it is observed how the oscillations in the top right corner are smoothed when the sample is refined, in addition with a reduction in the minimum of the pressure reached in the bottomost edges of the specimen. Therefore, it is concluded that the only discretization that does not show any visible oscillations

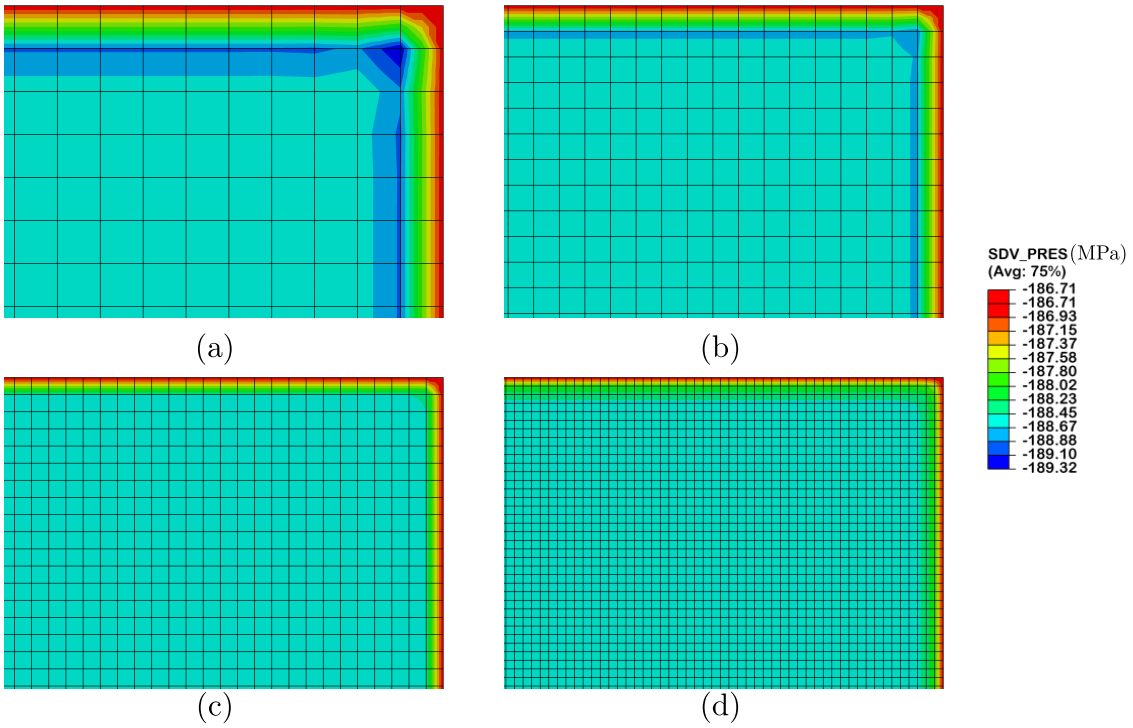

Figure 7: First increment of unloading pressure ramps conducted for discretizations with element sizes: (a) $h = 0.25$ mm, (b) $h = 0.15$ mm, (c) $h = 0.1$ mm and (d) $h = 0.05$ mm with a time step of $\Delta t = 0.5$ s. It is observed how by increasing discretization, the variation of the pressure becomes smooth.

is the finest one, $h = 0.05$ mm, proving this that the empirical condition of $h \leq \sqrt{D\Delta t}$ is required to ensure pressure stability of the sample.

Repeating the test, now for even a smaller time step: $\Delta t = 0.15$ s for a final unloading time of $t_f = 15$ s, we conduct again the tests for the different discretizations. According to the condition, the maximum element size to guarantee a stabilized simulation is $h_{\max} = 0.027$ mm. Therefore, none of the previous discretizations satisfy such constraint, so we will include in the simulations $h = 0.025$ mm. In line with the previous test, we commence by plotting the isocontours for pressure near the top right corner in Fig. 9 and we observe that as we decrease the time step, the observed oscillations are intensified for the coarser discretizations and further refinement is required to meet the conditions, leading it to a heavily refined model of 160,000 elements, that is characterized by a huge computational cost, meaning that reducing the time step leads to an increase of the computation time. The evolution of the pressure in the width of the thickness is quantified in Fig. 10 for a vertical path at the point $x = L - h$.

Having studied the diffusion length and subsequently proposed an empirical rule to tackle these instantaneous oscillations, it is worth highlighting another aspect that relies on the refinement of the mesh, but which is more visible during the swelling step: the appearance of swelling induced surface instabilities, a phenomenon due to the induction of compressive in-plane stresses. These instabilities have been deeply studied in the bibliography and have appeared in the form of creasing [72–75] and wrinkling [76, 77] in several experiments and numerical methods have addressed their appearance based on energy or equilibrium settings [56, 59, 78–82]. What is stated in the numerical approaches is that the appearance of these instabilities earlier during the swelling stage due to mesh refinement approaches the theoretical prediction of a instantaneous instability. Unlike the diffusion length issue, this phenomenon has been deeply addressed in the theory. Therefore, we just mention it here for the readers' consideration and do not address it further since we believe that the study of surface induced instabilities is out of the scope of the current investigation.

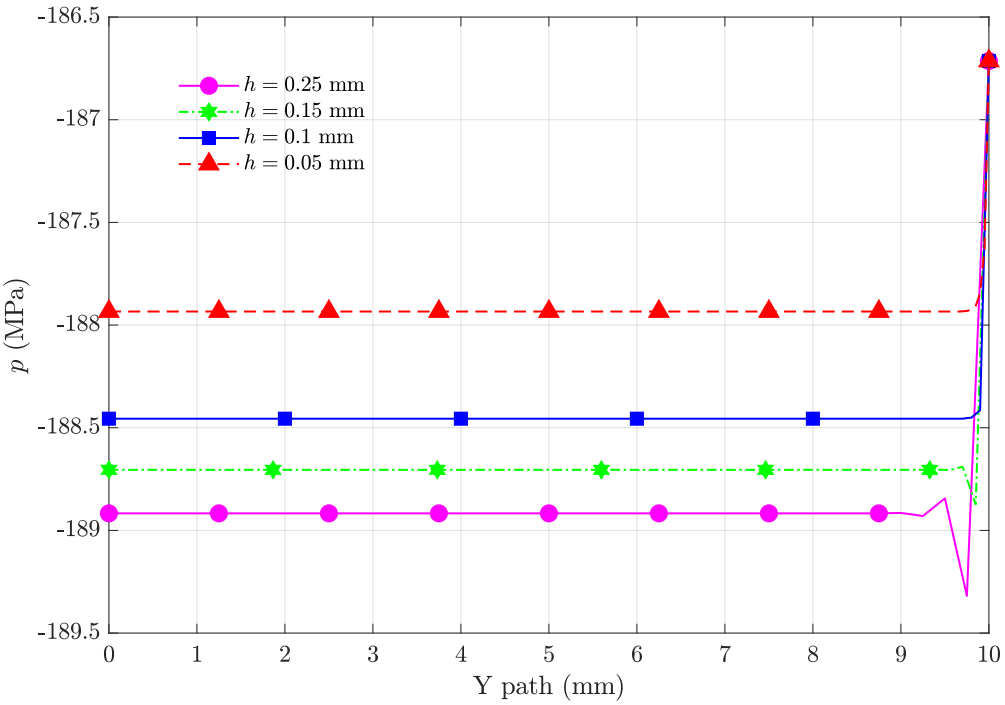

Figure 8: Evolution of the pressure for a vertical path in the sample at $x = L - h$ mm for different discretizations at the first increment of the pressure unloading step with a time step of $\Delta t = 0.5$ s. Oscillations in pressure are observed for coarser meshes near the top right corner.

5.1.3. Influence in temperature terms of displacement and pressure field

The additional particularity to be addressed is the inclusion of the last two terms in Eq. (66c), i.e., the temperature variation due to fluid flow and elastic stretching. The referential works of Chester and Anand [44] claims that both terms could be dismissed due to their relative minor influence on the hydrogel behavior compared to the other terms on the residual terms. This statement has been proven to be in line with other tests conducted for thermo-mechanical simulations of polymers such as [83, 84]. In the context of hydrogels, our investigations have unveiled that both terms significantly influence material behavior, primarily because of their mechanical properties, characterized by their notably low stiffness compared to other polymers. Such interplay of mechanical and thermal properties plays a major role in swelling experiments like [61, 85, 86]. In order to address this claim, the comparison between the swelling-deswelling results of Section 5.1.1 is conducted with and without considering these coupling terms. The isocontours for the temperature field at the beginning of the swelling step can be seen in Fig. 11. When both terms are neglected, an isothermal condition is observed. However, when both terms are considered, a significant temperature gradient of approximately 8 units of temperature is located at the top right corner of the square block. If we were running this analysis near the critical temperature T_c, such gradient could cause the transition of the LCST which will lead to a dramatic change of the solvent capacity to make the hydrogel swell. Therefore, the consideration of these terms cause, by taking a look just on the temperature field itself, significant thermal changes that alter the swelling behavior, which can be explained by the instantaneous change from a poor to good solvent and viceversa. Based on this argument the thermal fields should not be dismissed.

In addition to this, we pay attention on the time evolution of the displacement in the top right node during the full test on Fig. 12 and we observe that, now in the mechanical field, there are also some influences in the material behavior. It is observed how the trajectory for both tests is slightly different between both approaches, reaching a 5% difference on the peak of the specimen, and decaying quicker

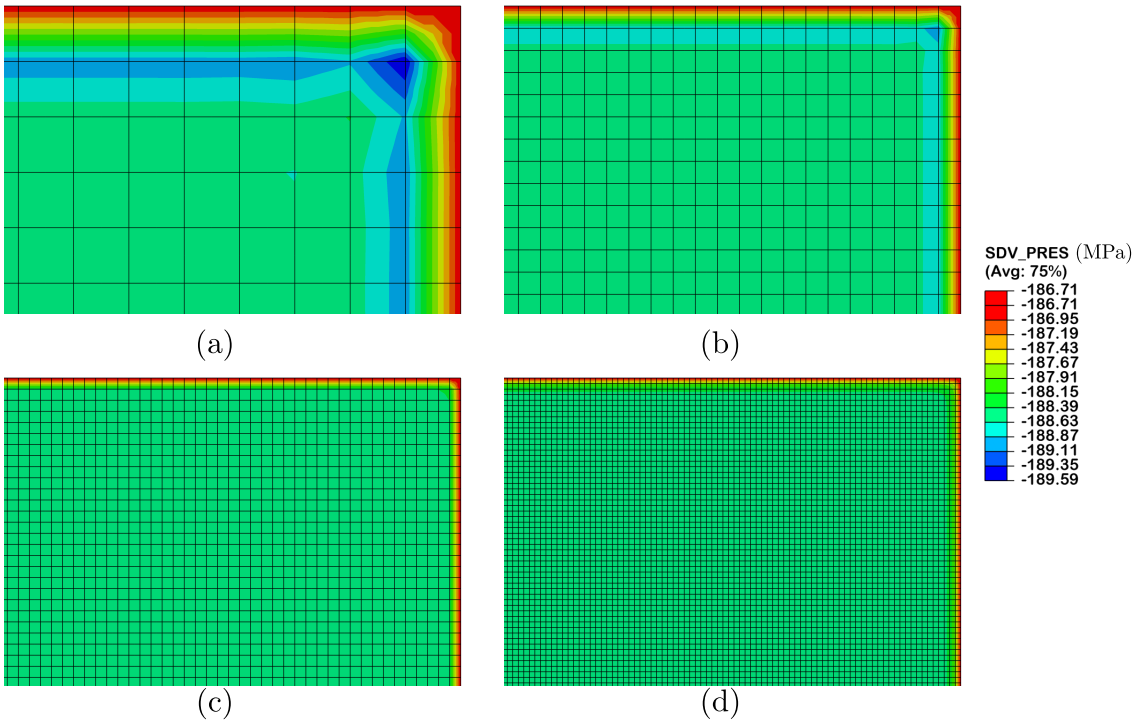

Figure 9: First increment of unloading pressure ramps conducted for discretizations with element sizes: (a) $h = 0.15$ mm, (b) $h = 0.1$ mm, (c) $h = 0.05$ mm and (d) $h = 0.025$ mm with a time step of $\Delta t = 0.15$ s. It is observed how by increasing discretization, the variation of the pressure becomes smooth.

during the deswelling stage for the full model. In addition to this, on numerical terms, it is important to highlight that the convergence of the approach considering both influences is more enhanced than the one dismissing both terms, which leads to more difficulties on conducting the test. Considering the distinct performances that are displayed here, we have presented some robust arguments to encourage the usage of a full formulation considering all the involved terms.

5.2. Free swelling + compression tests on agarose spheres

After the validation of the functionality of the proposed framework and addressed its particularities, we will focus on the remainder of the paper to show the ability of our model to replicate some complex test conditions for hydrogels. In the light of this idea, this Section is dedicated to analyzing the compression-based mechanical behavior of agarose hydrogels, which belong to the UCST gel category. For illustrative purposes, the micrographs taken showing the evolution of an agarose hydrogel during a experimental compression test are displayed in Fig. 13(a)-13(c). As we are delving into modeling thermoresponsive hydrogels, the authors have found compelling the investigation of compression results with respect to the temperature of the hydrogel. Therefore, to satisfy such requirements, the following test conditions are applied:

- It is modelled as the eighth of a three-dimensional sphere (symmetry conditions are prescribed in the X, Y and Z planes).
- Initial BCs for pressure with p_0 are applied to the whole domain with the fixed edges prescribed to a zero fluid flux.
- The entire body is prescribed to a temperature T_0 that is different for every conducted test. This is performed to account the differences in swelling and compression behavior for all the specimens. No isothermal conditions are considered, i.e., $\mathbf{Z} \neq 0$.

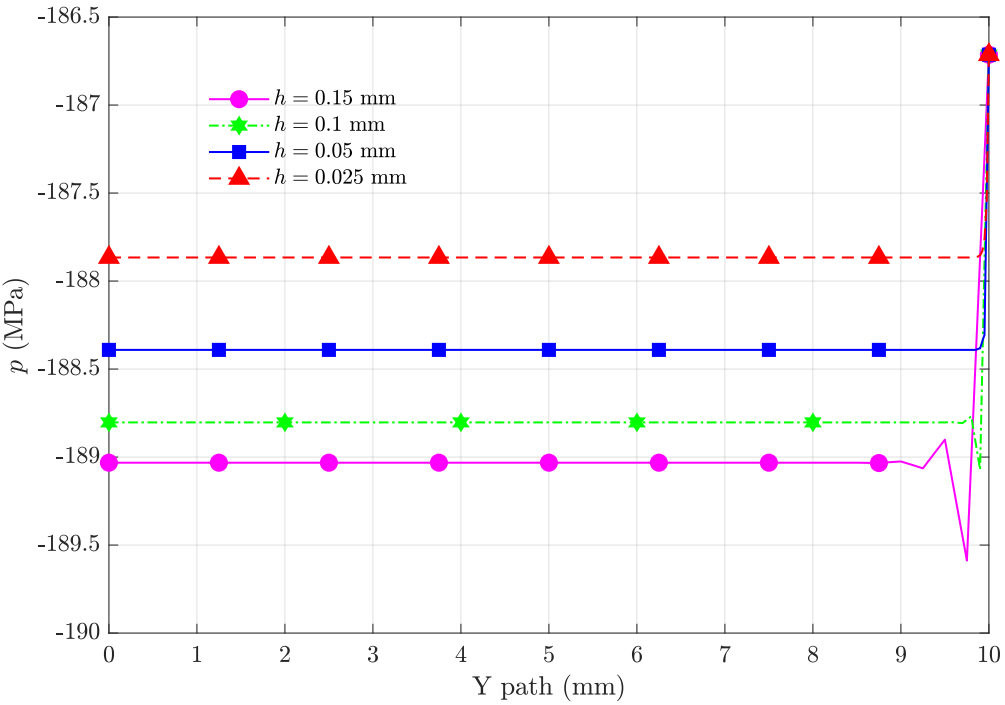

Figure 10: Evolution of the pressure for a vertical path in the sample at $x = L - h$ mm for different discretizations at the first increment of the pressure unloading step with a time step of $\Delta t = 0.15$ s. Oscillations in pressure are observed for coarser meshes near the top right corner.

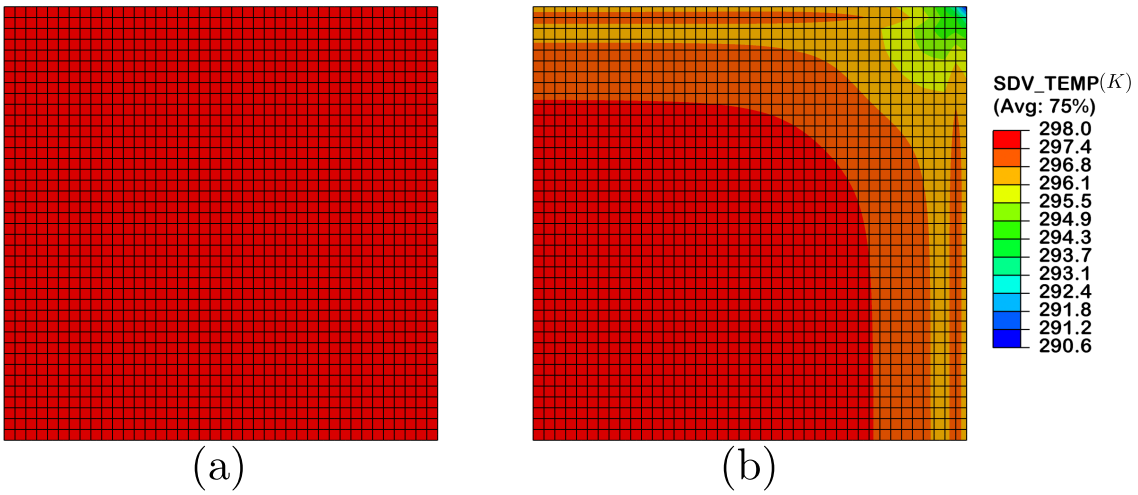

Figure 11: Isocontour displaying the temperature field (a) without and (b) with considering the fluid flow and elastic stretching influence on the temperature.

The material properties used to perform these analyses are plotted in Tab. 2. The layout of the problem is presented in Fig. 14, where we can visualize two instances in the problem of contact: a rectangular-shaped

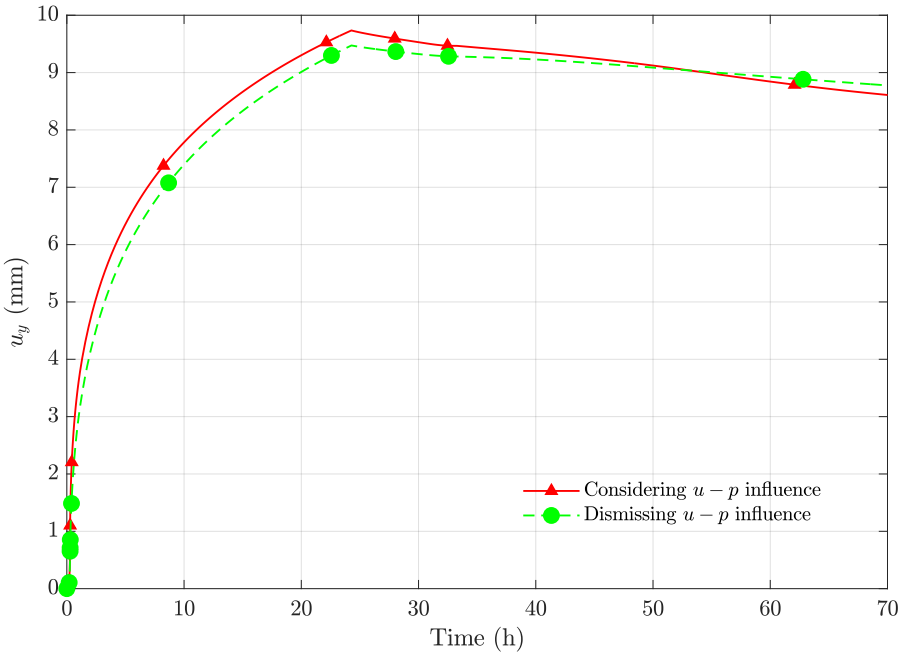

Figure 12: Time evolution of the vertical displacement in the top right node for the swelling-deswelling test with (red, continuous line) and without (green, dashed line) considering the fluid flow and elastic stretching influence on the temperature.

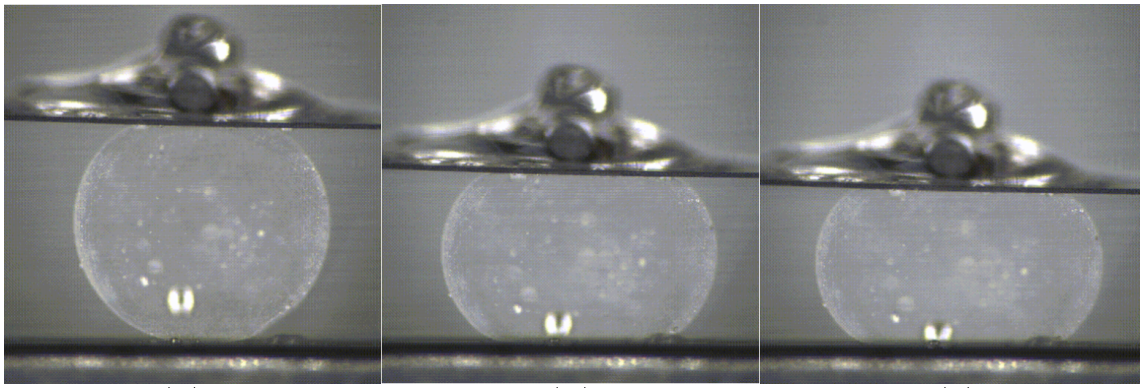

Figure 13: For illustrative purposes, the evolution of an agarose compression experimental test is presented.

plate modelled as a rigid solid that will act as the compressive load applier (it corresponds to the metallic item exhibited in Fig. 13) on the hydrogel sphere of radius $R = 5$ mm with a mesh of 432 20-node `Q2Q1Q1`; both instances are separated by a considerable distance to let the hydrogel swell freely without contacting the plate. The main goal of these analysis is to check how the swelling degree affects the compression tests, in terms of material behavior and maximum displacement reached in the experiment. For that purpose, the numerical test is divided into the following stages:

- First step consists in the pressure decrease at the edges that are in contact with the solvent. This is achieved via a linear ramp in $t = 300$ s from p_0 to 0 MPa with a fixed time increment of $\Delta t = 10$ s. The choice of such test conditions meet the condition to avoid pressure oscillations established in

Table 2: Material properties employed for the 3-D sphere subject to a compression test.

μ (MPa)	χ_L	χ_H	T_c (K)	Δ (K)	D (mm^2/s)	c_p $\left(\text{J}/(\text{mm}^3 \cdot \text{K})\right)$	α (K^{-1})	K $\left(\text{W}/(\text{mm}\cdot\text{K})\right)$	λ_0
0.35	0.1	0.7	320	5	5×10^{-2}	5.02	73×10^{-6}	0.35×10^{-3}	1.01

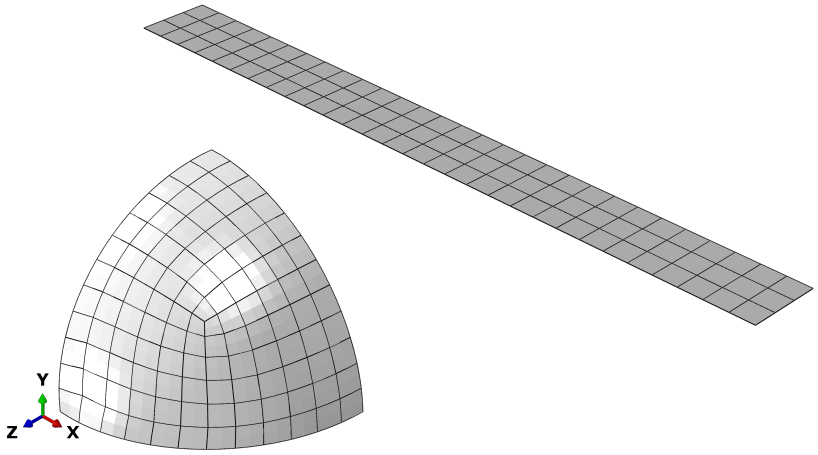

Figure 14: Geometry and mesh adopted for the numerical simulation of the compression test.

Section 5.1.2.

- For the next stage, the solid is subject to free transient swelling for 24 h.
- Subsequently, it is applied the quick compression test. With a displacement rate of $v = 10$ mm/s and a experiment time of $t = 1$ s, the rigid solid applies the compressive loading on the swollen hydrogel sphere following the conditions observed in Fig. 13.

We have studied the swelling-compression behavior of this sphere for the following range of initial temperatures: $T_0 = [305, 310, 315, 318, 319, 320, 321, 322, 325, 330, 335]$ K. In Figs. 15(a)-15(f), the evolution of this experiment is illustrated for the specimen at 315 K. The micrographs depicted in Figs. 15(a)-15(c) capture the swelling of the specimen during the initial stages when it comes into contact with the solvent and subsequently begins to grow due to fluid diffusion within the gel. Then, Fig. 15(d) represents the next stage of the numerical experiment, wherein rigid plates are introduced in contact with the sphere, and, as observed in the subsequent Figs. 15(e)-Fig. 15(f), they start compressing it, with a gradual increase of the stiffness of the sphere until it approaches infinity, ultimately ending the test. The similarities with the experiment plotted in Fig. 13 can be observed within these numerical simulations, with the small exception that in here we have a rigid plate compressing the sphere by both top and bottom surfaces.

For the record, Fig. 16 portrays a collection of curves concerning various magnitudes. First, to account that we manage to capture the UCST behavior, we have depicted the progression of the maximum displacement achieved during the swelling phase in Fig. 16(a). It is observed that the curves for tests with higher initial temperatures reach significantly higher peak values, thus proving the correlation between temperature and the swelling rate, which starts augmenting after $T > T_c$, as $\chi \sim \chi_H$.

Moving forward, the attention is now devoted to the mechanical response during the compression test. As Fig. 15 states, the compressive load is applied in the Y-direction. Therefore, in Figs. 16(b)-16(c), it is provided a representation concerning the time evolution of both peak normal (u_y) and transversal (u_x) nodal displacements. Initially, the displacement values starts to augment at an earlier stage for specimens with higher initial temperatures. This serves as compelling proof of the UCST behavior, as these samples have experienced more growth during the swelling phase. Consequently, the compressive force from the plates is

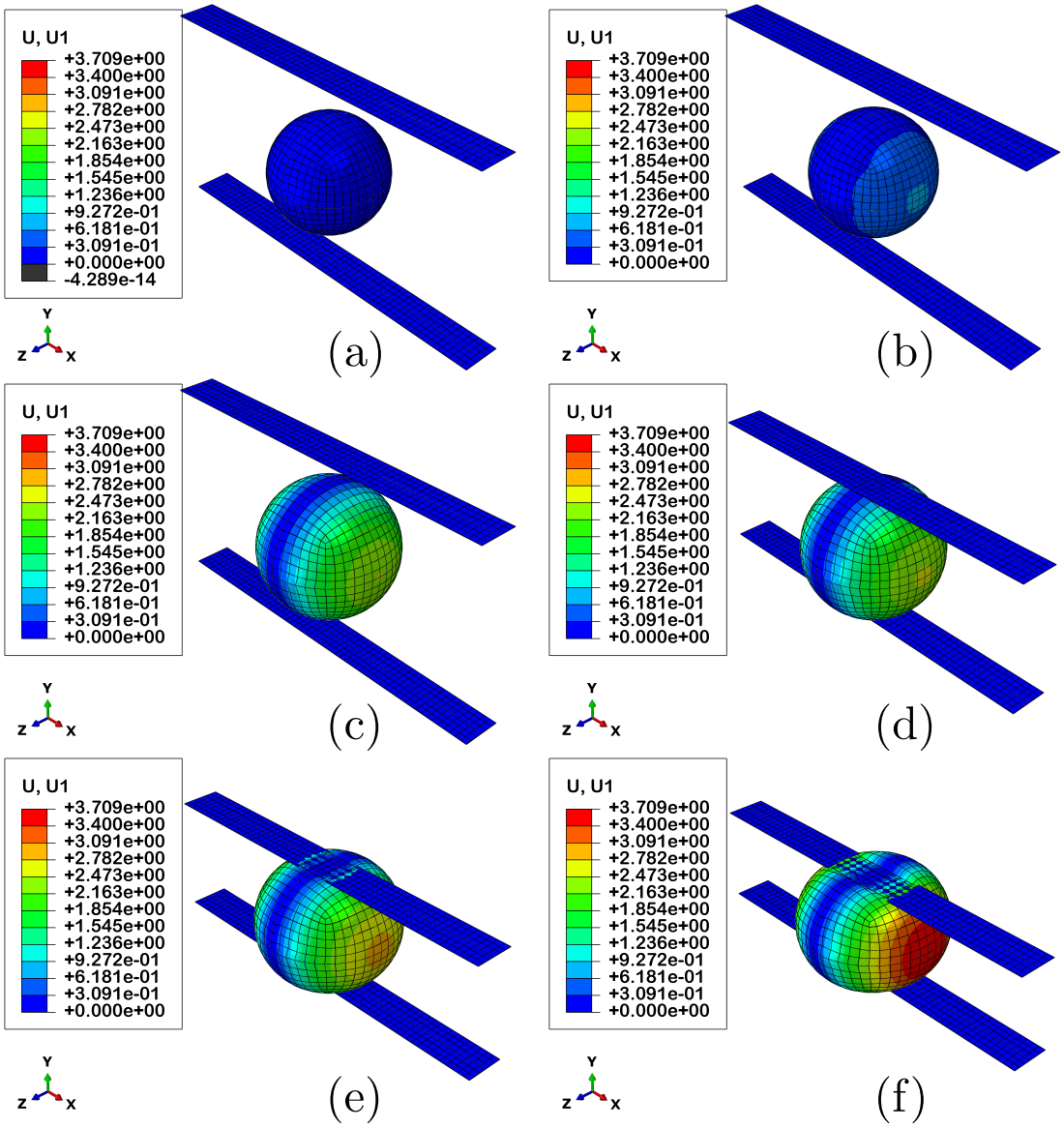

Figure 15: Steps of the swelling-compression example at 315K: states for (a) 0 s and (b) 300 s depict the decrease of pressure in the edges in contact with the solvent, (c) shows the subsequent swelling stage running for 24 hours, while (d)-(f) display the evolution of the quick compression test happening in the lapse of a second. Represented within these plots is the displacement u_x.

applied to them sooner in the process. Subsequently, as the volume of the specimen is smaller for lower T_0, the maximum value for displacement reached is also smaller. The reason behind this is that the point at which the stiffness of the sphere becomes nearly infinite is attained earlier, thereby prematurely concluding the test. The reaction force versus time curves, as depicted in Fig. 16(d), provide further confirmation of this observation, with their slope displaying a noticeable exponential behavior, which tends toward higher values for specimens with $T > T_c$. These series of swelling with compression tests have not only proven the reliability and versatility of our modeling framework for conducting experiments with UCST samples but also highlight its plausible integration with mechanical tests that can be experimentally compared and correlated with universal testing machines.

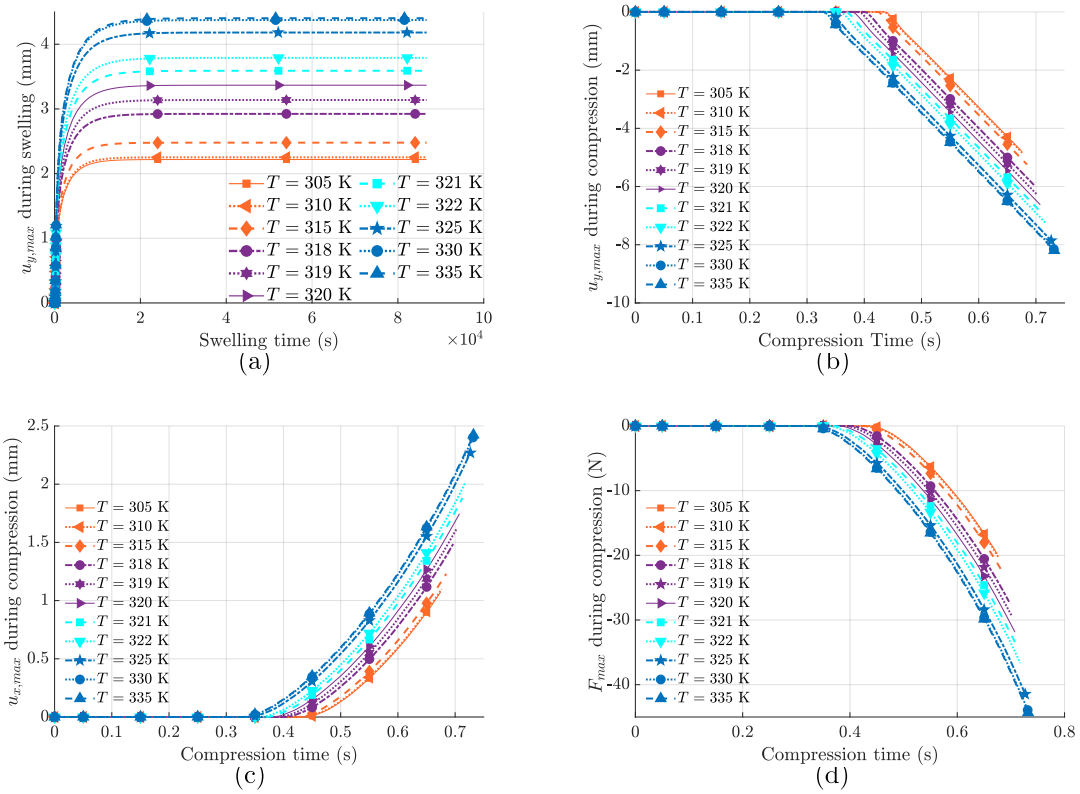

Figure 16: Graphs illustrating the evolution of multiple variables, ordered as follow: (a) maximum u_y attained during the swelling phase, (b) maximum nodal u_y, (c) maximum nodal u_x and (d) maximum nodal reaction force achieved during compression time.

5.3. Experimental correlation: free swelling of PNIPAAm hydrogels

Ultimately, important efforts have been devoted in establishing a quantitative correlation with the experimental data reported by [63], where they study the effect of crosslinking density on the swelling behavior for *PNIPAAm* hydrogels for different temperatures.

It is well-known that the *PNIPAAm*/water system show the type of swelling for a LCST hydrogel. Therefore, for this system, Oh et al. [63] synthetized various *N*-isopropylacrylamide (NIPA) gel particles with various crosslinking concentrations and measured the free swelling behavior of these materials to predict the swelling equilibrium of the hydrogel/solvent system. The magnitude that they employ to measure the degree of swelling is the volume ratio of gel particles. Their study shows that, for temperatures below the LCST, hydrogels with less crosslinking density become considerably more swollen. However, when the temperature is increased above the LCST, the influence of the crosslinking density is almost negligible, as the volume that this systems grow is considerably minor compared to cooler temperatures.

Heading back to the current modelling framework, in order to capture this experimental behavior and correlate with the main findings of [63], we propose the following approach: As the experimental work gives not enough details regarding the geometry and dimensions of the sample, we assume that the authors mean that the swelling properties do not depend on these characteristics, but in the material itself. Therefore, we have modelled one-eighth of a 3-D square block swelling of 20x20x20 mm, imposing symmetry conditions on the X, Y and Z plane. The employed properties are plotted in Tab. 3, based on the modelled material in [44].

Imposed chemical BCs are quite similar with respect to those defined in Section 5.1.1 during loading and swelling steps, but now for 3-D: symmetry surfaces are imposed zero flux conditions, whereas in the

Table 3: Material properties employed for the 3-D block under free transient swelling conditions.

μ (MPa)	χ_L	χ_H	T_c (K)	Δ (K)	D (mm^2/s)	c_p $\left(\text{J}/(\text{mm}^3 \cdot \text{K})\right)$	α (K^{-1})	K $\left(\text{W}/(\text{mm}\cdot\text{K})\right)$	λ_0
0.4	0.05	0.85	305	5	5×10^{-2}	5.02	73×10^{-6}	0.35×10^{-3}	1.01

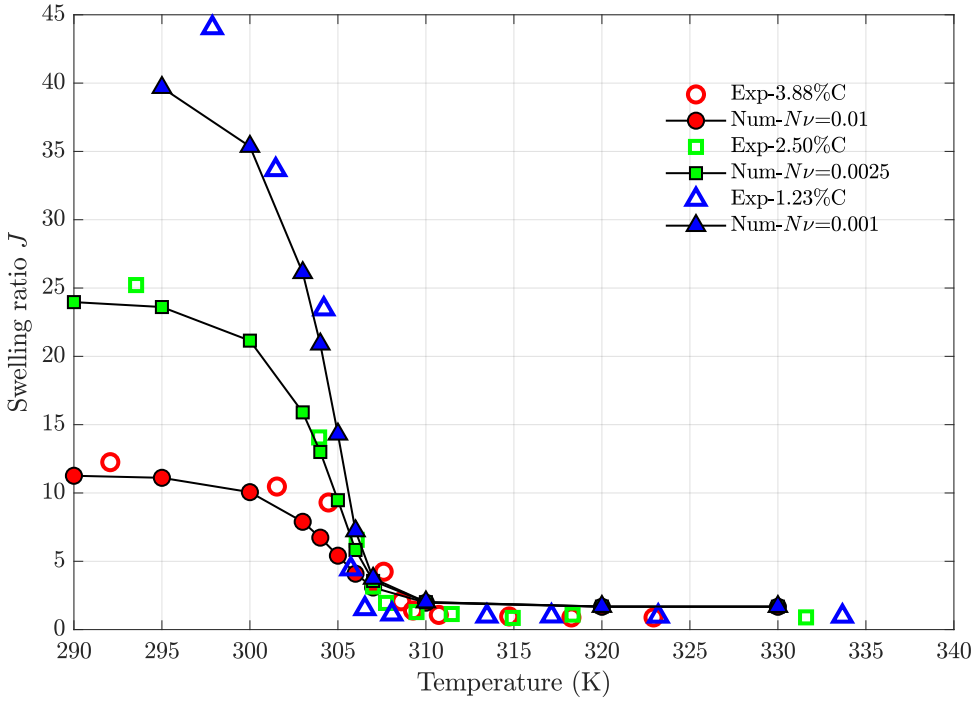

Figure 17: Volume of free-swelling hydrogel depending on temperature for different crosslinking densities. To adjust for the different experiments of [63], we have changed the parameter $N\nu$.

surfaces in contact with the solvent, a pressure of $p_0 = 0$ MPa is prescribed for an initial swelling ratio of $\lambda_0 = 1.01$, meaning that they are in equilibrium with the solvent. As the temperature has to remain constant for the whole analysis for proper correlation with the experiments, isothermal BCs are applied for the whole domain, meaning that $\mathbf{Z} = 0$. In accordance with the mesh sensitivity analysis carried out in Section 5.1.2, a mesh of 8,000 20-node `Q2Q1Q1` elements is employed for the whole analysis.

The parameter of our model that is related to the crosslinking density of our model is $N\nu$; therefore, it is the one to be adjusted to capture the experimental results. To compare with the experimental results that refer to volume change, we have plotted in Fig. 17 the Jacobian J on the swollen state under equilibrium (remember that is the magnitude that maps the volume variation from the reference configuration to the current one like $\mathrm{d}v = J\mathrm{d}V$) in front of the imposed temperature on the hydrogel. Experimental results study a experimental crosslinking of 1.23%, 2.50% and 3.88% and we have calibrated such change by controlling the $N\nu$ parameter following [87]. The results reveal that when reducing the $N\nu$ parameter, that is equivalent to reducing the crosslinking and then, the swelling ratio J of the hydrogel increases considerably when cooled below the LCST for both numerical and experimental tests. In addition to this, above the LCST, it is observed how the numerical and experimental results for the three analyzed samples do coincide, meaning the independence of this parameter when the hydrogel is heated above this temperature. Overall, it can be observed a strong correlation between the experiments and the numerical model, proving the solidness that the proposed framework provides in capturing the behavior of thermoresponsive hydrogels.

6. Conclusions

We have presented in this work an inf-sup stable mixed element for the modelling of thermoresponsive hydrogels in the form of a `UEL` subroutine. Specifically, we have adapted a mixed displacement-temperature-fluid pressure theory for its FE implementation. In order to achieve fulfillment of the LBB conditions and thus, gain inf-sup stability, we have adopted a quadratic interpolation for the displacement field and a linear interpolation for the temperature and the fluid pressure fields, thus employing a `Q2Q1Q1` formulation.

First, the functionality of the `Q2Q1Q1` element has been tested by analyzing a free swelling state followed by a subsequent deswelling caused by a temperature gradient in a LCST square block gel, performing very solidly. Subsequently, the dependence of the diffusion length on the mesh, a topic that has hastily been covered, has been evaluated by checking the pressure variations in the specimen, proving the importance of picking an appropiate discretization to avoid any visible oscillations in the fluid pressure. To conclude the verification part, we have compared the importance in the free swelling behavior of the temperature variation due to fluid flow and elastic stretching, coupled terms that have been ignored in the referential works due to their minor influence; we have found that due to the low stiffness that hydrogels present, such terms should be considered for an appropiate swelling test, not only in terms of accuracy, but also in convergence.

Subsequently, our research has been extended to more complex experiments. Initially, we have successfully delved into the compressive behavior of UCST swollen spheres, studying the effect that the initial temperature of each hydrogel poses into the mechanical behavior of such gels. Moreover, the model has achieved accuracy in capturing experimental results by correlating the effect of the cross-linking density on the swelling behavior for *PNIPAAm* hydrogels, varying temperature.

Future efforts with this formulation will be devoted towards the implementation of a model for fracture of thermoresponsive hydrogels that can be experimentally tested. As part of this investigation, the recently developed mixed formulation for incompressible hyperelastic materials [88] combined with the F-bar method could be exploited for this purpose. The study of the structural integrity of hydrogels holds a particular significance, especially in the applications of tissue engineering and drug delivery systems.

Acknowledgments

AVG and JR appreciate the financial support of the Ministerio de Ciencia e Innovación de España (Project TED2021-131649B-I00). BD acknowledges funding from the National Science Foundation through the DMREF program under grant number CMMI 2119716.

References

[1] D. J. Beebe, J. S. Moore, J. M. Bauer, Q. Yu, R. H. Liu, C. Devadoss, B. H. Jo, Functional hydrogel structures for autonomous flow control inside microfluidic channels, Nature 404 (6778) (2000) 588–590. doi:https://doi.org/10.1038/35007047.

[2] J. Wang, Z. Chen, M. Mauk, K.-S. Hong, M. Li, S. Yang, H. H. Bau, Self-actuated, thermo-responsive hydrogel valves for lab on a chip, Biomedical Microdevices 7 (4) (2005) 313–322. doi:https://doi.org/10.1007/s10544-005-6073-z.

[3] S. E. Bakarich, R. Gorkin III, M. i. h. Panhuis, G. M. Spinks, 4d printing with mechanically robust, thermally actuating hydrogels, Macromolecular Rapid Communications 36 (12) (2015) 1211–1217. doi:https://doi.org/10.1002/marc.201500079.

[4] D. Buenger, F. Topuz, J. Groll, Hydrogels in sensing applications, Progress in Polymer Science 37 (12) (2012) 1678–1719. doi:https://doi.org/10.1016/j.progpolymsci.2012.09.001.

[5] Y. Guan, Y. Zhang, Boronic acid-containing hydrogels: synthesis and their applications, Chem. Soc. Rev. 42 (2013) 8106–8121. doi:http://dx.doi.org/10.1039/C3CS60152H.

[6] G. Cai, J. Wang, K. Qian, J. Chen, S. Li, P. S. Lee, Extremely stretchable strain sensors based on conductive self-healing dynamic cross-links hydrogels for human-motion detection, Advanced Science 4 (2) (2017) 1600190. doi:https://doi.org/10.1002/advs.201600190.

[7] Y.-J. Liu, W.-T. Cao, M.-G. Ma, P. Wan, Ultrasensitive wearable soft strain sensors of conductive, self-healing, and elastic hydrogels with synergistic "soft and hard" hybrid networks, ACS Applied Materials & Interfaces 9 (30) (2017) 25559–25570. doi:https://doi.org/10.1021/acsami.7b07639.

[8] J. L. Drury, D. J. Mooney, Hydrogels for tissue engineering: scaffold design variables and applications, Biomaterials 24 (24) (2003) 4337–4351, synthesis of Biomimetic Polymers. doi:https://doi.org/10.1016/S0142-9612(03)00340-5.

[9] G. Chan, D. J. Mooney, New materials for tissue engineering: towards greater control over the biological response, Trends Biotechnol 26 (7) (2008) 382–392. doi:https://doi.org/10.1016/j.tibtech.2008.03.011.
[10] M. Jamal, S. S. Kadam, R. Xiao, F. Jivan, T.-M. Onn, R. Fernandes, T. D. Nguyen, D. H. Gracias, Bio-origami hydrogel scaffolds composed of photocrosslinked peg bilayers, Advanced Healthcare Materials 2 (8) (2013) 1142–1150. doi:https://doi.org/10.1002/adhm.201200458.
[11] N. Annabi, A. Tamayol, J. A. Uquillas, M. Akbari, L. E. Bertassoni, C. Cha, G. Camci-Unal, M. R. Dokmeci, N. A. Peppas, A. Khademhosseini, 25th anniversary article: Rational design and applications of hydrogels in regenerative medicine, Adv Mater 26 (1) (2014) 85–123. doi:https://doi.org/10.1002/adma.201303233.
[12] R. Dinarvand, A. D'Emanuele, The use of thermoresponsive hydrogels for on-off release of molecules, Journal of Controlled Release 36 (3) (1995) 221–227. doi:https://doi.org/10.1016/0168-3659(95)00035-7.
[13] Y. Qiu, K. Park, Environment-sensitive hydrogels for drug delivery, Advanced Drug Delivery Reviews 53 (3) (2001) 321–339, triggering in Drug Delivery Systems. doi:https://doi.org/10.1016/S0169-409X(01)00203-4.
[14] N. Peppas, J. Hilt, A. Khademhosseini, R. Langer, Hydrogels in biology and medicine: From molecular principles to bionanotechnology, Advanced Materials 18 (11) (2006) 1345–1360. doi:https://doi.org/10.1002/adma.200501612.
[15] J. Li, D. J. Mooney, Designing hydrogels for controlled drug delivery, Nature Reviews Materials 1 (12) (2016) 16071. doi:https://doi.org/10.1038/natrevmats.2016.71.
[16] H. R. Culver, J. R. Clegg, N. A. Peppas, Analyte-responsive hydrogels: Intelligent materials for biosensing and drug delivery, Accounts of Chemical Research 50 (2) (2017) 170–178. doi:https://doi.org/10.1021/acs.accounts.6b00533.
[17] D. Schmaljohann, Thermo- and ph-responsive polymers in drug delivery, Advanced Drug Delivery Reviews 58 (15) (2006) 1655–1670, 2006 Supplementary Non-Thematic Collection. doi:https://doi.org/10.1016/j.addr.2006.09.020.
[18] A. Richter, G. Paschew, S. Klatt, J. Lienig, K.-F. Arndt, H.-J. P. Adler, Review on hydrogel-based ph sensors and microsensors, Sensors 8 (1) (2008) 561–581. doi:https://doi.org/10.3390/s8010561.
[19] T. Tanaka, D. Fillmore, S.-T. Sun, I. Nishio, G. Swislow, A. Shah, Phase transitions in ionic gels, Phys. Rev. Lett. 45 (1980) 1636–1639. doi:https://doi.org/10.1103/PhysRevLett.45.1636.
[20] T. Tanaka, I. Nishio, S.-T. Sun, S. Ueno-Nishio, Collapse of gels in an electric field, Science 218 (4571) (1982) 467–469. doi:https://doi.org/10.1126/science.218.4571.467.
[21] A. Suzuki, T. Tanaka, Phase transition in polymer gels induced by visible light, Nature 346 (6282) (1990) 345–347. doi:https://doi.org/10.1038/346345a0.
[22] R. Brighenti, M. P. Cosma, Mechanics of multi-stimuli temperature-responsive hydrogels, Journal of the Mechanics and Physics of Solids 169 (2022) 105045. doi:https://doi.org/10.1016/j.jmps.2022.105045.
[23] R. A. Barry, P. Wiltzius, Humidity-sensing inverse opal hydrogels, Langmuir 22 (3) (2006) 1369–1374. doi:https://doi.org/10.1021/la0519094.
[24] Y. Liu, L. Wang, M. Zhang, D. Tu, X. Mao, Y. Liao, Long-period grating relative humidity sensor with hydrogel coating, IEEE Photonics Technology Letters 19 (12) (2007) 880–882. doi:https://doi.org/10.1109/LPT.2007.897551.
[25] L. E. Bromberg, E. S. Ron, Temperature-responsive gels and thermogelling polymer matrices for protein and peptide delivery, Advanced Drug Delivery Reviews 31 (3) (1998) 197–221, peptide Release from Polymer Matrices. doi:https://doi.org/10.1016/S0169-409X(97)00121-X.
[26] S. R. Sershen, S. L. Westcott, N. J. Halas, J. L. West, Temperature-sensitive polymer–nanoshell composites for photothermally modulated drug delivery, Journal of Biomedical Materials Research 51 (3) (2000) 293–298. doi:https://doi.org/10.1002/1097-4636(20000905)51:3¡293::AID-JBM1¿3.0.CO;2-T.
[27] M. E. Harmon, M. Tang, C. W. Frank, A microfluidic actuator based on thermoresponsive hydrogels, Polymer 44 (16) (2003) 4547–4556. doi:https://doi.org/10.1016/S0032-3861(03)00463-4.
[28] B. Jeong, S. W. Kim, Y. H. Bae, Thermosensitive sol–gel reversible hydrogels, Advanced Drug Delivery Reviews 64 (2012) 154–162. doi:https://doi.org/10.1016/j.addr.2012.09.012.
[29] L. Klouda, Thermoresponsive hydrogels in biomedical applications: A seven-year update, European Journal of Pharmaceutics and Biopharmaceutics 97 (2015) 338–349, polymers for Drug Delivery Systems. doi:https://doi.org/10.1016/j.ejpb.2015.05.017.
[30] L. Altomare, L. Bonetti, C. E. Campiglio, L. De Nardo, L. Draghi, F. Tana, S. Farè, Biopolymer-based strategies in the design of smart medical devices and artificial organs, Int J Artif Organs 41 (6) (2018) 337–359. doi:https://doi.org/10.1177/0391398818765323.
[31] T. Gotoh, Y. Nakatani, S. Sakohara, Novel synthesis of thermosensitive porous hydrogels, Journal of Applied Polymer Science 69 (5) (1998) 895–906. doi:https://doi.org/10.1002/(SICI)1097-4628(19980801)69:5¡895::AID-APP8¿3.0.CO;2-H.
[32] J. Zhang, L.-Y. Chu, Y.-K. Li, Y. M. Lee, Dual thermo- and ph-sensitive poly(n-isopropylacrylamide-co-acrylic acid) hydrogels with rapid response behaviors, Polymer 48 (6) (2007) 1718–1728. doi:https://doi.org/10.1016/j.polymer.2007.01.055.
[33] S. Cai, Z. Suo, Mechanics and chemical thermodynamics of phase transition in temperature-sensitive hydrogels, Journal of the Mechanics and Physics of Solids 59 (11) (2011) 2259–2278. doi:https://doi.org/10.1016/j.jmps.2011.08.008.
[34] S. Ashraf, H.-K. Park, H. Park, S.-H. Lee, Snapshot of phase transition in thermoresponsive hydrogel pnipam: Role in drug delivery and tissue engineering, Macromolecular Research 24 (4) (2016) 297–304. doi:https://doi.org/10.1007/s13233-016-4052-2.
[35] N. Bhattarai, H. R. Ramay, J. Gunn, F. A. Matsen, M. Zhang, Peg-grafted chitosan as an injectable thermosensitive hydrogel for sustained protein release, Journal of Controlled Release 103 (3) (2005) 609–624. doi:https://doi.org/10.1016/j.jconrel.2004.12.019.
[36] W. Wu, J. Shen, P. Banerjee, S. Zhou, Core–shell hybrid nanogels for integration of optical temperature-sensing, targeted tumor cell imaging, and combined chemo-photothermal treatment, Biomaterials 31 (29) (2010) 7555–7566. doi:https://doi.org/10.1016/j.biomaterials.2010.06.030.

[37] G. Vancoillie, D. Frank, R. Hoogenboom, Thermoresponsive poly(oligo ethylene glycol acrylates), Progress in Polymer Science 39 (6) (2014) 1074 – 1095. doi:https://doi.org/10.1016/j.progpolymsci.2014.02.005.
[38] J. Dolbow, E. Fried, H. Ji, Chemically induced swelling of hydrogels, Journal of the Mechanics and Physics of Solids 52 (1) (2004) 51–84. doi:https://doi.org/10.1016/S0022-5096(03)00091-7.
[39] H. Ji, H. Mourad, E. Fried, J. Dolbow, Kinetics of thermally induced swelling of hydrogels, International Journal of Solids and Structures 43 (7) (2006) 1878–1907. doi:https://doi.org/10.1016/j.ijsolstr.2005.03.031.
[40] W. Hong, X. Zhao, J. Zhou, Z. Suo, A theory of coupled diffusion and large deformation in polymeric gels, Journal of the Mechanics and Physics of Solids 56 (5) (2008) 1779–1793. doi:https://doi.org/10.1016/j.jmps.2007.11.010.
[41] W. Hong, Z. Liu, Z. Suo, Inhomogeneous swelling of a gel in equilibrium with a solvent and mechanical load, International Journal of Solids and Structures 46 (17) (2009) 3282–3289. doi:https://doi.org/10.1016/j.ijsolstr.2009.04.022.
[42] M. K. Kang, R. Huang, A Variational Approach and Finite Element Implementation for Swelling of Polymeric Hydrogels Under Geometric Constraints, Journal of Applied Mechanics 77 (6) (08 2010). doi:https://doi.org/10.1115/1.4001715.
[43] S. A. Chester, L. Anand, A coupled theory of fluid permeation and large deformations for elastomeric materials, Journal of the Mechanics and Physics of Solids 58 (11) (2010) 1879–1906. doi:https://doi.org/10.1016/j.jmps.2010.07.020.
[44] S. A. Chester, L. Anand, A thermo-mechanically coupled theory for fluid permeation in elastomeric materials: Application to thermally responsive gels, Journal of the Mechanics and Physics of Solids 59 (10) (2011) 1978–2006. doi:https://doi.org/10.1016/j.jmps.2011.07.005.
[45] Z. Ding, W. Toh, J. Hu, Z. Liu, T. Y. Ng, A simplified coupled thermo-mechanical model for the transient analysis of temperature-sensitive hydrogels, Mechanics of Materials 97 (2016) 212–227. doi:https://doi.org/10.1016/j.mechmat.2016.02.018.
[46] J. Hu, N. Jiang, J. Du, Thermally controlled large deformation in temperature-sensitive hydrogels bilayers, International Journal of Smart and Nano Materials 12 (4) (2021) 450–471. doi:https://doi.org/10.1080/19475411.2021.1958091.
[47] X. Zhang, S. Chumakov, X. Li, M. Klinsmann, S. U. Kim, C. Linder, J. Christensen, An Electro-chemo-thermo-mechanical Coupled Three-dimensional Computational Framework for Lithium-ion Batteries, Journal of The Electrochemical Society 167 (2020) 160542. doi:10.1149/1945-7111/abd1f2.
[48] E. de Souza Neto, D. Perić, M. Dutko, D. Owen, Design of simple low order finite elements for large strain analysis of nearly incompressible solids, International Journal of Solids and Structures 33 (20) (1996) 3277–3296. doi:https://doi.org/10.1016/0020-7683(95)00259-6.
[49] I. Babuška, The finite element method with lagrangian multipliers, Numerische Mathematik 20 (3) (1973) 179–192. doi:https://doi.org/10.1007/BF01436561.
[50] F. Brezzi, On the existence, uniqueness and approximation of saddle-point problems arising from lagrangian multipliers, Revue française d'automatique, informatique, recherche opérationnelle. Analyse numérique 8 (R2) (1974) 129–151. doi:https://doi.org/10.1051/m2an/197408R201291.
[51] A. Krischok, C. Linder, A generalized inf–sup test for multi-field mixed-variational methods, Computer Methods in Applied Mechanics and Engineering 357 (2019) 112497. doi:10.1016/j.cma.2019.06.008.
[52] B. Dortdivanlioglu, A. Krischok, L. Beirão da Veiga, C. Linder, Mixed isogeometric analysis of strongly coupled diffusion in porous materials, International Journal for Numerical Methods in Engineering 114 (2018) 28–46. doi:10.1002/nme.5731.
[53] M. A. Murad, A. F. Loula, Improved accuracy in finite element analysis of biot's consolidation problem, Computer Methods in Applied Mechanics and Engineering 95 (3) (1992) 359–382. doi:https://doi.org/10.1016/0045-7825(92)90193-N.
[54] J. Wan, Stabilized finite element methods for coupled geomechanics and multiphase flow, Ph.D. thesis, United States – California (2003).
[55] A. Krischok, C. Linder, On the enhancement of low-order mixed finite element methods for the large deformation analysis of diffusion in solids, International Journal for Numerical Methods in Engineering 106 (4) (2016) 278–297. doi:https://doi.org/10.1002/nme.5120.
[56] N. Bouklas, C. M. Landis, R. Huang, A nonlinear, transient finite element method for coupled solvent diffusion and large deformation of hydrogels, Journal of the Mechanics and Physics of Solids 79 (2015) 21–43. doi:https://doi.org/10.1016/j.jmps.2015.03.004.
[57] N. Bouklas, C. M. Landis, R. Huang, Effect of Solvent Diffusion on Crack-Tip Fields and Driving Force for Fracture of Hydrogels, Journal of Applied Mechanics 82 (8) (08 2015). doi:https://doi.org/10.1115/1.4030587.
[58] C. Taylor, P. Hood, A numerical solution of the navier-stokes equations using the finite element technique, Computers & Fluids 1 (1) (1973) 73–100. doi:https://doi.org/10.1016/0045-7930(73)90027-3.
[59] B. Dortdivanlioglu, C. Linder, Diffusion-driven swelling-induced instabilities of hydrogels, Journal of the Mechanics and Physics of Solids 125 (2019) 38–52. doi:https://doi.org/10.1016/j.jmps.2018.12.010.
[60] M. Ilavský, J. Hrouz, K. Ulbrich, Phase transition in swollen gels, Polymer Bulletin 7 (2) (1982) 107–113. doi:https://doi.org/10.1007/BF00265460.
[61] M. Takekawa, E. Kokufuta, Swelling–shrinking behaviors of poly(n-isopropylacrylamide) and poly(n-n-propylacrylamide) gels prepared by chemical and radiation crosslinking methods, Colloid and Polymer Science 287 (3) (2009) 323–334. doi:https://doi.org/10.1007/s00396-008-1969-9.
[62] R. Kishi, A. Matsuda, T. Miura, K. Matsumura, K. Iio, Fast responsive poly(n, n-diethylacrylamide) hydrogels with interconnected microspheres and bi-continuous structures, Colloid and Polymer Science 287 (5) (2009) 505–512. doi:https://doi.org/10.1007/s00396-009-2002-7.
[63] K. S. Oh, J. S. Oh, H. S. Choi, Y. C. Bae, Effect of cross-linking density on swelling behavior of nipa gel particles, Macromolecules 31 (21) (1998) 7328–7335. doi:https://doi.org/10.1021/ma971554y.
[64] M. Ortiz, L. Stainier, The variational formulation of viscoplastic constitutive updates, Computer Methods in Applied Mechanics and Engineering 171 (3) (1999) 419–444. doi:https://doi.org/10.1016/S0045-7825(98)00219-9.

[65] Q. Yang, L. Stainier, M. Ortiz, A variational formulation of the coupled thermo-mechanical boundary-value problem for general dissipative solids, Journal of the Mechanics and Physics of Solids 54 (2) (2006) 401–424. doi:https://doi.org/10.1016/j.jmps.2005.08.010.
[66] C. Miehe, S. Mauthe, H. Ulmer, Formulation and numerical exploitation of mixed variational principles for coupled problems of cahn–hilliard-type and standard diffusion in elastic solids, International Journal for Numerical Methods in Engineering 99 (10) (2014) 737–762. doi:https://doi.org/10.1002/nme.4700.
[67] P. J. Flory, J. Rehner, Statistical mechanics of cross-linked polymer networks ii. swelling, The Journal of Chemical Physics 11 (11) (1943) 521–526. doi:https://doi.org/10.1063/1.1723792.
[68] M. L. Huggins, Solutions of long chain compounds, The Journal of Chemical Physics 9 (5) (1941) 440–440. doi:https://doi.org/10.1063/1.1750930.
[69] P. J. Flory, Thermodynamics of high polymer solutions, The Journal of Chemical Physics 10 (1) (1942) 51–61. doi:https://doi.org/10.1063/1.1723621.
[70] Q.-S. Yang, L.-H. Ma, J.-J. Shang, The chemo-mechanical coupling behavior of hydrogels incorporating entanglements of polymer chains, International Journal of Solids and Structures 50 (14) (2013) 2437–2448. doi:https://doi.org/10.1016/j.ijsolstr.2013.03.039.
[71] I. Babuska, B. A. Szabo, I. N. Katz, The p-version of the finite element method, SIAM Journal on Numerical Analysis 18 (3) (1981) 515–545. doi:https://doi.org/10.1137/0718033.
[72] E. Southern, A. G. Thomas, Effect of constraints on the equilibrium swelling of rubber vulcanizates, Journal of Polymer Science Part A: General Papers 3 (2) (1965) 641–646. doi:https://doi.org/10.1002/pol.1965.100030220.
[73] T. Tanaka, Kinetics of phase transition in polymer gels, Physica A: Statistical Mechanics and its Applications 140 (1) (1986) 261–268. doi:https://doi.org/10.1016/0378-4371(86)90230-X.
[74] V. Trujillo, J. Kim, R. C. Hayward, Creasing instability of surface-attached hydrogels, Soft Matter 4 (2008) 564–569. doi:http://dx.doi.org/10.1039/B713263H.
[75] J. Yoon, J. Kim, R. C. Hayward, Nucleation, growth, and hysteresis of surface creases on swelled polymer gels, Soft Matter 6 (2010) 5807–5816. doi:http://dx.doi.org/10.1039/C0SM00372G.
[76] T. Tanaka, S.-T. Sun, Y. Hirokawa, S. Katayama, J. Kucera, Y. Hirose, T. Amiya, Mechanical instability of gels at the phase transition, Nature 325 (6107) (1987) 796–798. doi:https://doi.org/10.1038/325796a0.
[77] M. Guvendiren, J. A. Burdick, S. Yang, Solvent induced transition from wrinkles to creases in thin film gels with depth-wise crosslinking gradients, Soft Matter 6 (2010) 5795–5801. doi:https://dx.doi.org/10.1039/C0SM00317D.
[78] M. K. Kang, R. Huang, Swell-induced surface instability of confined hydrogel layers on substrates, Journal of the Mechanics and Physics of Solids 58 (10) (2010) 1582–1598. doi:https://doi.org/10.1016/j.jmps.2010.07.008.
[79] Z. Wu, N. Bouklas, R. Huang, Swell-induced surface instability of hydrogel layers with material properties varying in thickness direction, International Journal of Solids and Structures 50 (3) (2013) 578–587. doi:https://doi.org/10.1016/j.ijsolstr.2012.10.022.
[80] W. Toh, Z. Ding, T. Yong Ng, Z. Liu, Wrinkling of a Polymeric Gel During Transient Swelling, Journal of Applied Mechanics 82 (6) (06 2015). doi:https://doi.org/10.1115/1.4030327.
[81] F. Xu, M. Potier-Ferry, A multi-scale modeling framework for instabilities of film/substrate systems, Journal of the Mechanics and Physics of Solids 86 (2016) 150–172. doi:https://doi.org/10.1016/j.jmps.2015.10.003.
[82] A. Ilseng, V. Prot, B. H. Skallerud, B. T. Stokke, Buckling initiation in layered hydrogels during transient swelling, Journal of the Mechanics and Physics of Solids 128 (2019) 219–238. doi:https://doi.org/10.1016/j.jmps.2019.04.008.
[83] P. K. A. V. Kumar, A. Dean, S. Sahraee, J. Reinoso, M. Paggi, Non-linear thermoelastic analysis of thin-walled structures with cohesive-like interfaces relying on the solid shell concept, Finite Elements in Analysis and Design 202 (2022) 103696. doi:https://doi.org/10.1016/j.finel.2021.103696.
[84] Z. Liu, J. Reinoso, M. Paggi, Hygro-thermo-mechanical modeling of thin-walled photovoltaic laminates with polymeric interfaces, Journal of the Mechanics and Physics of Solids 169 (2022) 105056. doi:https://doi.org/10.1016/j.jmps.2022.105056.
[85] J. Pleštil, M. Ilavský, H. Pospíšil, D. Hlavatá, Y. Ostanevich, G. Degovics, M. Kriechbaum, P. Laggner, Saxs, sans and photoelasticity of poly(n,n-diethylacrylamide) networks: 1. structure changes after temperature jumps, Polymer 34 (23) (1993) 4846–4851. doi:https://doi.org/10.1016/0032-3861(93)90008-X.
[86] A. Drozdov, Mechanical behavior of temperature-sensitive gels under equilibrium and transient swelling, International Journal of Engineering Science 128 (2018) 79–100. doi:https://doi.org/10.1016/j.ijengsci.2018.03.009.
[87] C. G. Lopez, W. Richtering, Does flory–rehner theory quantitatively describe the swelling of thermoresponsive microgels?, Soft Matter 13 (2017) 8271–8280. doi:http://dx.doi.org/10.1039/C7SM01274H.
[88] A. Valverde-González, J. Reinoso, B. Dortdivanlioglu, M. Paggi, Locking treatment of penalty-based gradient-enhanced damage formulation for failure of compressible and nearly incompressible hyperelastic materials, Computational Mechanics 72 (4) (2023) 635–662. doi:https://doi.org/10.1007/s00466-023-02314-x.